

AN XMM-NEWTON OBSERVATION OF THE GALAXY GROUP NGC 5044: ABUNDANCE PROFILES, INTRINSIC ABSORPTION, AND IMPLICATIONS.

David A. Buote¹, Aaron D. Lewis¹, Fabrizio Brighenti^{2,3}, & William G. Mathews²
Submitted to The Astrophysical Journal 1/27/02

ABSTRACT

We present a detailed initial analysis of a new XMM observation of the bright nearby galaxy group NGC 5044, which has been previously interpreted as a massive cooling flow. Outside of the central 1° (10 kpc) region the diffuse X-ray emission is approximately circular. Within a 1° radius the emission displays asymmetries which the archival Chandra image reveals to be holes similar to those seen in other cooling flows. To obtain the spherically averaged three-dimensional properties of the diffuse gas we perform a simultaneous spatial-spectral deprojection analysis of the EPIC MOS CCD data. Assuming a single-phase gas in each spatial bin we find that the 3D temperature profile rises outwards from $T = 0.75$ keV at the center to $T = 1.2$ keV at $r = 50$ kpc and then declines slowly until reaching a value of $T = 1.1$ keV at $r = 100$ kpc similar to the profile obtained with ROSAT. Within the central 30 kpc, where the temperature is changing rapidly, the quality of the deprojected fits is notably superior to their traditional un-deprojected counterparts. Moreover, using a simple gaussian or flat emission measure model within the three inner 1° -wide spatial bins we measure in each bin the narrow temperature distribution expected for the single-phase temperature gradient. A standard multiphase cooling flow, which implies a much wider temperature distribution, is a poor fit to the XMM data.

The Fe abundance exhibits a prominent gradient where $Z_{\text{Fe}} = 1Z$ within $r = 5^{\circ}$ (50 kpc) and falls to $Z_{\text{Fe}} = 0.35Z$ at $r = 100$ kpc. The near-solar values obtained within the inner regions confirm that the very sub-solar Fe abundances obtained previously for NGC 5044 are the result of an "Fe Bias" arising from fitting isothermal models to multi-temperature spectra. In particular, we reproduce previous ASCA results and demonstrate explicitly the Fe Bias for NGC 5044 by fitting models to the MOS spectra accumulated within a circle of radius 5° . Consequently, the "Iron Discrepancy" raised by Arimoto et al. can be attributed partially to previous incorrect X-ray measurements of Fe abundances due to the Fe Bias.

Models without intrinsic absorption give Mg/O ratios of $5 - 7$ solar in the central bins which substantially exceed the values of 0.8-0.9 solar expected from both SN Ia and SN II. (The Si/O ratios are also too large for the measured Si/Fe ratio.) Only a warm absorber ($T = 0.01$ keV) gives Mg/O ratios near solar ($1.2 - 1.4$ solar) consistent with SN enrichment (as well as consistent Si/O and Si/Fe ratios). The success of the warm absorber model is manifested not only by lowering the Mg abundance but also by increasing the oxygen abundance to $Z_{\text{O}} = 0.6Z$ in the central bins and by providing the best fits there of any model we investigated. We discuss the serious theoretical problems posed by a warm absorber which might indicate instead that it is merely a surrogate for another physical or instrumental effect that is masquerading as an absorber.

The apparent absence of multiphase cooling in NGC 5044 is incompatible with traditional gas dynamical models that are globally flowing inward, but the modest central metal enrichment observed in NGC 5044 is also incompatible with outflowing models.

Finally, we report a high energy excess within the central 1 arcmin bin of the MOS data that is consistent with a power law with photon index ≈ 2 . But the origin of this emission is unclear since the Chandra image reveals that the hard emission does not arise from a central point source.

Subject headings: X-rays: galaxies: clusters { galaxies: halos { galaxies: formation { cooling flows

1. introduction

The extended X-ray emission surrounding isolated elliptical galaxies provides a wealth of astronomical information about the past history of galaxy formation and supernova enrichment. Studies of the metallicity in rich clusters constrain the number of SN II and SN Ia events per unit L_B . However, much of this information, contained in the radial abundance variations around individual galaxies,

is lost when groups combine to form rich clusters. In contrast, the relatively undisturbed X-ray gas in isolated, centrally dominated groups can preserve in its radial distribution unique information about the time sequence of star formation and supernovae events from the earliest times. The hot gas around isolated E galaxies is expected to be enriched and heated by SN II-driven galactic winds from group members before they merged to create the cen-

¹ Department of Physics and Astronomy, University of California at Irvine, 4129 Frederick Reines Hall, Irvine, CA 92697-4575

² UCO/Lick Observatory, University of California, Santa Cruz, CA 95064

³ Dipartimento di Astronomia, Università di Bologna, via Ranzani 1, Bologna 40127, Italy

tral E galaxy. Longer lasting, less powerful winds driven by SN Ia explosions are expected in galaxies and bulges of modest or low mass. The real fossil information lies not in the central galaxy, but in the metal enrichment in the surrounding X-ray emitting gas.

Unfortunately, reliable constraints on the metal enrichment in such systems are lacking because the metal abundances in the hot gas in isolated (massive) E-galaxies and centrally E-dominated groups determined from previous X-ray studies have yielded conflicting results with most authors finding very sub-solar Fe abundances in the central regions (see Buote 1999, 2000a, and references therein). These low Fe abundances are generally less than the stellar values which likely implies little or no enrichment from SN Ia and thus an IMF much flatter than that of the Milky Way (e.g., Arimoto et al. 1997; Renzini 1997; Wyse 1997). In contrast, in our analyses of the ASCA data accumulated within $r \leq 3^{\circ}$ of the brightest ellipticals and groups we found that the Fe abundances are approximately solar and that the previous inferences of very sub-solar Fe abundances using ASCA data are the result of a bias arising from assuming the gas to be isothermal in the presence of significant radial temperature gradients (Buote & Fabian 1998; Buote 1999, 2000a). We obtained similar results from a spatial-spectral deprojection analysis of the ROSAT data of these systems (Buote 2000c).

Some previous ROSAT and ASCA studies of "cooling flow" galaxies and groups also found evidence for intrinsic absorbing material located preferentially near the centers of these systems. In particular, in Buote (2000d) we showed that previous discrepancies between ROSAT and ASCA studies could be reconciled if the absorber is "warm" such that $T = 10^5$ – 10^6 K. Unfortunately, neither ROSAT nor ASCA had the combined spatial and spectral resolution to place accurate constraints on the spatial distribution and detailed physical properties (e.g., temperature) of the intrinsic absorber.

To address these issues we have obtained an XMM observation of NGC 5044, perhaps the brightest nearby galaxy group in X-rays. (We adopt an angular-diameter distance of 38.6 Mpc to NGC 5044 corresponding to $z = 0.00898$ and assuming $H_0 = 70 \text{ km s}^{-1} \text{ Mpc}^{-1}$ and $\Omega_0 = 0.3$.) The XMM EPIC CCDs essentially combine the best capabilities of ROSAT and ASCA; i.e., the spatial resolution of ROSAT and the spectral resolution of ASCA. NGC 5044 was observed during AO1 for 20 ks as part of the XMM GO program (PIMATHES). In this paper we present initial detailed results of the temperatures, metal abundances, and absorption properties obtained from a spatial-spectral deprojection analysis of the data taken with the EPIC MOS camera (Struder et al. 2001). We also present initial interpretations of these results using theoretical gas-dynamical models. The EPIC pn data give results essentially consistent with the MOS, but because of some issues with the pn background subtraction (see x4.4) we defer its presentation to a follow-up paper that will also include a simultaneous analysis of the public Chandra ACIS-S data⁴.

A major objective of this paper is to demonstrate the

care required in measuring spectral parameters, especially abundances and absorption column densities, from broadband spectral fits to the medium resolution CCD data. We show that the standard spectral model consisting of a single coronal plasma component modified by foreground Galactic absorption yields good qualitative fits in each annulus. The largest fractional deviations of the model from the data typically are only 20%–30% in each spectral bin. However, the χ^2 deviations are quite significant, and the super-solar M g/O ratios obtained from these models are not consistent with supernova enrichment. We explore increasingly more complex models until we obtain the best possible fits and physical M g/O ratios. During this investigation we identify and constrain spectral regions of possible calibration error and possible intrinsic errors in the plasma codes.

The paper is organized as follows. In x2 we present the observations and discuss the data reduction. We summarize the spatial-spectral deprojection analysis in x3. A analysis using the standard single-phase model with no intrinsic absorption is presented in x4. Multitemperature models are discussed in x5. We discuss models that include intrinsic absorption in x6. Possible non-thermal emission within the central arcminute is discussed in x7. Implications of the measured abundance profiles for gas-dynamical models of the enrichment of the hot gas are discussed in x8. We present our conclusions in x9.

2. observations and data preparation

We generated a calibrated events list using the standard SAS v5.2.0 software (task: emchain). Inspection of the light curves of the MOS1 and MOS2 for data with energies above 10 keV revealed no large gaps. By excluding time intervals corresponding to count rates greater than 10 counts per 27 s bin (and also performing the standard screening criteria) we obtained total exposures of 22510 s and 22572 s for the MOS1 and MOS2 respectively.

In Figure 1 we display an adaptively smoothed MOS1 image. Several sources can be seen embedded in the diffuse emission which fills the entire MOS field. That we see more sources at large radius suggests that discrete sources at smaller radii are swamped by the diffuse emission which is brightest near the center. Outside of the central 1° region the diffuse emission is approximately circular. The centroid of the X-ray surface brightness within 2° – 3° radius is slightly offset from the centroid near 5° – 6° radius (i.e., the edge of the central MOS field) noted previously in the ROSAT PSPC observation of NGC 5044 (David et al. 1994); at larger radius the centroids appear to coincide with the centroid at the smallest radii.

Although not obvious from Figure 1, a careful inspection of the MOS and pn images within $R \leq 1^{\circ}$ of NGC 5044 reveals significant non-circular features. To better observe these features we also display in Figure 1 the higher resolution archival Chandra ACIS-S image of NGC 5044. (We cleaned the 20 ks ACIS-S observation of gaps and selected the standard ASCA event grades using the standard CIAO software.) The Chandra image exhibits holes in the hot gas similar to those seen in other Chandra images of the cores of groups and clusters (e.g., Fabian et al. 2000; M c-

⁴ We note that our focus is on the CCD data because only the CCDs are able to probe the spectral data at radii larger than 0.5° and provide spatially resolved spectra (though see Xu et al. (2001) who have discussed a method to extract some spatial information from the RGS data via a Monte Carlo method.

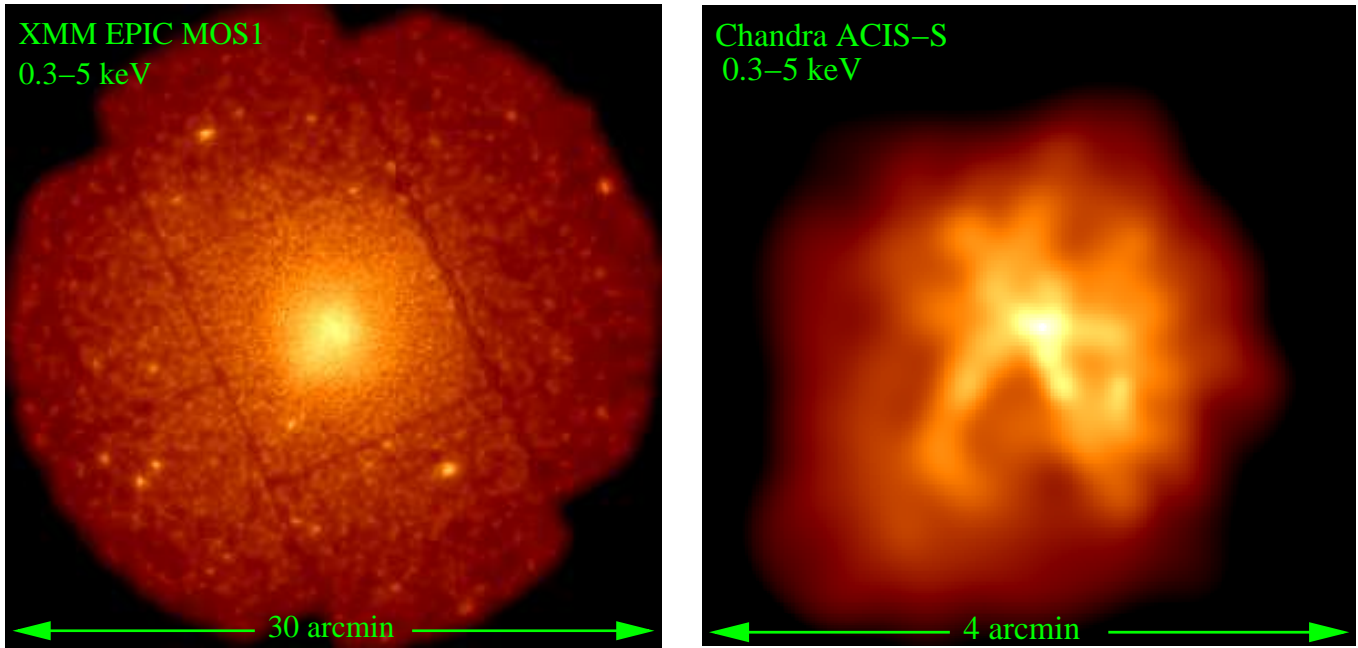


Fig. 1. (Left panel) False-color XMM MOS1 image of NGC 5044 adaptively smoothed using the SAS task `asmooth`. (Right panel) Portion of the archival Chandra ACIS-S image (also false-color) located at the center of NGC 5044 adaptively smoothed using the CIAO task `csmooth`.

Namara et al. 2000; Churazov et al. 2001).

Since the diffuse emission of NGC 5044 fills the entire MOS field of view we estimate the background using the standard "background templates". These templates are event lists obtained by combining several high Galactic latitude pointings⁵. Since the quiescent background can vary typically by $\sim 10\%$ it is necessary to normalize the background templates to each source observation. Since NGC 5044 has a gas temperature ~ 1 keV there is little emission from hot gas for energies > 5 keV. Consequently, we normalized the MOS1 and MOS2 background templates by comparing source and background counts in the 7-12 keV band extracted from regions near the edges of the MOS fields. (Limitations in the accuracy of this background estimate are discussed in §4.4.)

We extracted spectra in concentric circular annuli located at the X-ray centroid of the inner contours (i.e., computed within a 2° radius) such that the width of each annulus contained ~ 5000 background-subtracted counts in the 0.3-5 keV band in each MOS detector, and the minimum width was set to 1° for PSF considerations. Obvious point sources were masked out before the extraction (and corresponding regions also were omitted from the background templates). These restrictions resulted in a total of nine annuli within $r = 12^\circ$. (Note that the results we present below are quite insensitive to the choice of centroid; e.g., if instead the image centroid computed for radii $5^\circ \leq r \leq 12^\circ$ is used.)

RMF and ARF files were generated using SAS. (Note that the vignetting correction is administered through the ARF file.) Finally, the spectral pulse-invariant (PI) files for each annulus were rebinned such that each energy bin contains a minimum of 30 counts appropriate for χ^2 fitting.

3. spatial-spectral deprojection analysis

To obtain the three-dimensional properties of the X-ray emitting gas we perform a deprojection analysis assuming spherical symmetry using the (non-parametric) "onion-peeling" technique. That is, one begins by determining the spectral model in the bounding annulus and then works inwards by subtracting off the spectral contributions from the outer annuli. Whereas most previous studies have emphasized spectral-blind "image" deprojection, or have merely deprojected the emission-weighted parameters obtained from the 2D analysis, we have developed a code based on `xspec` (Arnaud 1996) to perform the proper spatial-spectral analysis (Buote 2000c). Consequently, we obtain temperatures, abundances, densities, and absorption column densities (and any other desired parameters) by fitting spectral models to the "deprojected spectra". By that we really mean that to the spectrum extracted from a 2D annulus ($R_{i-1}; R_i$) on the sky we fit a two-component model consisting of the spectral contribution from the 3D shell with the same inner and outer radii as the 2D annulus ($r_{i-1} = R_{i-1}; r_i = R_i$) plus the contribution projected into the 2D annulus from 3D shells exterior to the shell in question ($r_{j-1} > r_i; r_j$). The assumption of spherical symmetry is justified by the nearly round X-ray image for $R \leq 10^\circ$.

In this procedure we account for the emission projected from shells outside of our bounding annulus by assuming the X-ray emissivity for such shells varies as a power-law with radius and has the same spectral shape as determined from the bounding annulus. For the XMM data for NGC 5044 we take the radial surface brightness to vary as r^{-2} (or $\alpha = 0.5$ for the model) as indicated by the data within $R = 10^\circ$. As found previously (e.g. Buote 2000c) the derived spectral parameters (except

⁵ See XMM calibration note by D. Lumb (XMM-SOC-CAL-TN-0016).

density in the penultimate annulus) are quite insensitive to this choice.

To estimate the uncertainties on the fitted parameters we simulated spectra for each annulus using the best-fitting models and fit the simulated spectra in exactly the same manner as done for the actual data. From 100 Monte Carlo simulations we compute the standard deviation for each free parameter which we quote as the $\pm 1\sigma$ error. (This is a slightly different manner of quoting the errors compared to $\times 3.2$ Buote 2000c.)

Because deprojection always introduces (radial) bin-to-bin fluctuations we regularize (i.e., smooth) some of the parameters (see $\times 3.3$ of Buote 2000c). In actuality we regularize *ex post facto* by restricting the value of a parameter within certain bounds specified by a pre-determined radial variation for the parameter. As in our previous ROSAT study of NGC 5044 (Buote 2000c) we only regularize the abundances since they exhibit much larger bin-to-bin fluctuations than the temperatures. And as we discuss below in $\times 4.2$ we restrict the radial abundance variation such that the logarithmic derivative is between ± 2 .

We take the solar abundances in *xspec* (v11.1.0o) to be those given by the Anders & Grevesse (1989) table except for Fe where we use the correct "meteoritic" value, $Fe/H = 3.24 \times 10^{-5}$ by number, as suggested by Ishimaru & Arimoto (1997) and McWilliam (1997). This value is 1.44 times smaller than the photospheric value in Anders & Grevesse (1989) which is usually employed in X-ray spectral fitting. Consequently, we shall account for this factor when comparing our results to other studies.

4. standard model

We begin by studying what we shall term the "standard model" for the X-ray spectrum of a bright elliptical galaxy / galaxy group like NGC 5044. This model consists of thermal emission from a coronal plasma modified only by foreground Galactic absorption ($N_H^{Gal} = 5 \times 10^{20} \text{ cm}^{-2}$). This standard model assumes the gas is single-phase; i.e., the gas is described by a single temperature and density at each radius. In *xspec* we represent the absorption using the *phabs* model and the emission using the *apec*⁶ model. We focus on the *apec* code since it is the most up-to-date and (for the temperature ranges of interest here) includes the most emission lines. (Whenever we have used the *mekal* code we have found no qualitative differences with the results presented below.) In each *apec* model the free parameters are T , Fe , O , Ne , Mg , Si (S tied to Si in solar ratio), and normalization. All other elemental abundances are tied to Fe in their solar ratios. (Note that we tie S to Si to reduce the number of free parameters. In every fit we have investigated with Si and S untied the fitted values of Si and S are consistent.)

4.1. Temperature

In Figure 2 we show radial temperature profiles obtained with and without deprojection; the latter is the usual case where the spectrum collected from an annulus on the sky is fitted directly to the standard model. The definitions of these models and the χ^2 values of the fits in each annulus are given in Tables 1 and 2 respectively. Our fits include

only data between 0.3 and 5 keV since background dominates higher energies and the calibration is (presently) less certain at lower energies.

As can be seen in Figure 2 the temperature is minimum at the center (~ 0.7 keV) and rises to ~ 1.2 keV near $4''$ similar to previous determinations with ROSAT (David et al. 1994; Buote 2000c). Notice in particular that the deprojected model (i.e., B) fits much better than the 2D model (i.e., A) within the central three bins where the "true" 3D temperature is changing rapidly (Table 2). The deprojected temperature has a steeper rise outward from the center fully consistent with the 2D profile being smeared by projection effects. The lower temperature in the bounding radius certainly suggests a declining temperature value, but its value is itself underestimated because of projection; i.e., we have had to assume the projected emission from shells exterior to our bounding annulus has the same spectral shape as the bounding annulus ($\times 3$).

4.2. Fe Abundance and Fe Bias

The Fe abundance profiles for models without (A) and with (B) deprojection are displayed in the middle panel of Figure 2. In each case there is a clear gradient where $Z_{Fe} \sim 1Z$ near the center and $Z_{Fe} \sim 0.35Z$ in the bounding shell. However, the profile for model B has large fluctuations between bins at large radii. These large fluctuations and uncertainties are primarily the result of even larger fluctuations and uncertainties in O , Ne , and Mg (not shown) since if these elements are tied to Fe in their solar ratios a much smoother profile results quite similar to that of model A for bins 5-9. Consequently, as discussed at the beginning of $\times 3$ we perform regularization *ex post facto* by restricting the bin-to-bin variation of the abundances such that the radial logarithmic derivative lies between ± 2 . This value was selected to minimize the bin-to-bin Fe fluctuations while also insuring that the values within the inner 1-2 bins were consistent with the unsmoothed values and that the 3D Fe profile is not smoother than the 2D profile of model A. (This slope is also much larger than the logarithmic slope of ~ 0.4 obtained from a line connecting the Fe values of the central and bounding bins for model B.)

The result is plotted as model C in the right panel of Figure 2. Although qualitatively similar, it is evident that the 3D Fe profile consistently exceeds the 2D Fe values by 10% -20% for bins 1-5. The smaller Fe values for model A are the result of two effects: (1) the projection of low-Fe gas from shells at larger radii, and (2) the "Fe Bias".

Previously we have argued that the very sub-solar Fe abundances computed within $r \lesssim 5''$ using ROSAT and ASCA observations of nearby elliptical galaxies and galaxy groups are caused by an "Fe Bias" (see Buote 2000a,c). This bias is the result of forcing an isothermal model to fit a multi-temperature spectrum with average temperature near 1 keV. The combined spatial and spectral resolution of the XMM-MOS CCDs allows a vivid demonstration of this bias.

For this exercise we extracted the MOS spectra within circles of $R = 5''$ as we did in our previous analysis of the ASCA data of NGC 5044 in Buote (1999). Then we fitted isothermal (1T) and two-temperature (2T) models to

⁶ <http://hea-www.harvard.edu/APEC/>

Table 1
Model Definitions

Model	Component Type	Component Name	Deprojected (Y/N)	Annuli	Comments
A	absorption	phabs	N	1-9	$N_H = N_H^{\text{Gal}}$
A	emission	vapec	N	1-9	no regularization
B	absorption	phabs	N	1-9	$N_H = N_H^{\text{Gal}}$
B	emission	vapec	Y	1-9	no regularization
C	absorption	phabs	N	1-9	$N_H = N_H^{\text{Gal}}$
C	emission	vapec	Y	1-9	
D	absorption	phabs	N	1-9	$N_H = N_H^{\text{Gal}}$
D	emission	vapec	Y	4-9	
D	emission	vapec_gauss	Y	1-3	
E	absorption	phabs	N	1-9	
E	emission	vapec	Y	1-9	
F	absorption	phabs	N	1-9	
F	emission	vapec	Y	4-9	
F	emission	vapec_gauss	Y	1-3	
G	absorption	phabs	N	1-9	$N_H = N_H^{\text{Gal}}$
G	absorption	zphabs	N	1-7	$z = 0:00898$
G	emission	vapec	Y	1-9	
H	absorption	phabs	N	1-9	$N_H = N_H^{\text{Gal}}$
H	absorption	zphabs	N	1-7	$z = 0:00898$
H	emission	vapec	Y	4-9	
H	emission	vapec_gauss	Y	1-3	
I	absorption	phabs	N	1-9	$N_H = N_H^{\text{Gal}}$
I	absorption	warmabs	N	1-7	$z = 0:00898, T = 0:01 \text{ keV}$
I	emission	vapec	Y	1-9	
J	absorption	phabs	N	1-9	$N_H = N_H^{\text{Gal}}$
J	absorption	warmabs	N	1-7	$z = 0:00898, T = 0:01 \text{ keV}$
J	emission	vapec	Y	4-9	
J	emission	vapec_gauss	Y	1-3	

Note. | N_H^{Gal} is the Galactic hydrogen column density, $N_H = 5 \times 10^{20} \text{ cm}^{-2}$, obtained using the Goddard w3nh tool. In each emission model the free parameters are T , Fe , O , Ne , Mg , Si (S tied to Si in solar ratio), and normalization. All other elemental abundances are tied to Fe in their solar ratios. The gaussian emission measure (vapec_gauss) has the additional free parameter σ representing the standard deviation of the gaussian. See x4, x5.1, and x6 for further descriptions of these models.

Table 2
Quality of Spectral Fits (χ^2/dof)

Annulus	R_{in} (arcmin)	R_{out} (arcmin)	A	B	C	D
1	0.0	1.0	753.00/272	630.50/272	630.89/272	568.35/271
2	1.0	2.0	1129.53/296	703.68/296	706.02/296	553.54/295
3	2.0	3.0	559.67/290	484.92/290	491.91/290	414.21/289
4	3.0	4.0	446.85/279	448.53/279	447.82/279	
5	4.0	5.0	327.77/272	329.11/272	344.49/272	
6	5.0	6.0	245.72/250	245.18/250	253.15/250	
7	6.0	7.0	253.44/247	253.02/247	265.06/247	
8	7.0	8.3	303.72/259	304.62/259	320.06/259	
9	8.3	9.9	359.80/285	359.80/285	359.80/285	

Note. | See Table 1 for the model definitions A-D.

the spectra. Our default model is model A (Table 1) while the 2T model adds another apec component with variable temperature and normalization but abundances tied to the first component.

Fitting these models yields the following: $\chi^2 = 3383.8/433 \text{ dof}$ with $Z_{\text{Fe}} = Z = 0:63 \pm 0:01$ for 1T compared to $880.8/431$ and $Z_{\text{Fe}} = Z = 1:20 \pm 0:03$ for 2T. Notice first that the 2T model is a vast improvement in χ^2 quality over 1T. Second, over the $R = 5^0$ region the 1T value of Z_{Fe} severely underestimates the 3D emission-weighted value of Z_{Fe} . These effects we have defined previously as the "Fe Bias". (In fact, the inner bins of model C still suffer from some Fe Bias as shown below in x5.) If we restrict

the lower energy limit to 0.6 keV and use the old "photospheric" value for the solar Fe abundance appropriate for previous ASCA studies, we obtain $Z_{\text{Fe}} = Z = 0:22 \pm 0:01$ (1T) and $Z_{\text{Fe}} = Z = 0:53 \pm 0:03$ (2T). The 1T values are very similar to 1T models fitted to the ASCA data of N5044; e.g., $Z_{\text{Fe}} = Z = 0:32 \pm 0:02$ (Fukazawa et al. 1996) and $Z_{\text{Fe}} = Z = 0:22^{+0:35}_{-0:07}$ (Buote 1999). The 2T result is also fully consistent with our previous ASCA result of $Z_{\text{Fe}} = Z = 0:57^{+0:10}_{-0:08}$ (90% conf).

Hence, the XMM EPIC data confirm that previous very sub-solar Fe abundances obtained for NGC 5044 were the result of the Fe Bias. (And also the value of $Z_{\text{Fe}} = 0:35Z$ obtained by Finoguenov & Ponman 1999 was the result

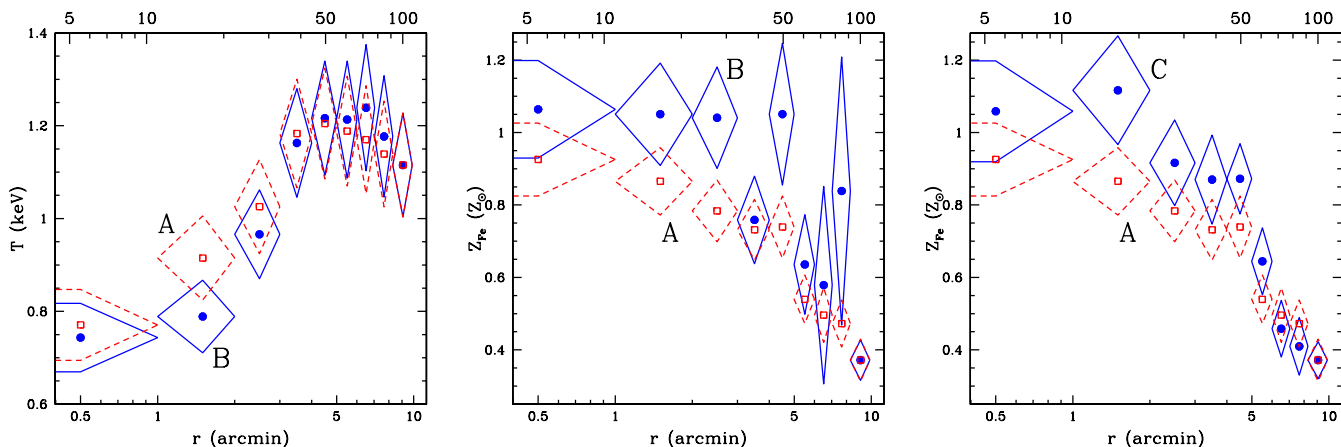


Fig. 2. (Left panel) Radial temperature profiles (units { bottom : arcminutes, top : kpc) and 1 σ errors for models defined in Table 1. (Middle panel) The iron abundance profiles of these models. (Right panel) Smoothed Fe abundance profile obtained from deprojected analysis (model C) compared to (unsmoothed) values of the 2D model (model A).

of over-regularization as suggested in section 5.2 of Buote 2000c.) Note that the Fe Bias observed for model A in Figure 2 is smaller than described for the $R = 5^{\circ}$ region for the same reasons why our previous ROSAT analysis did not show a large Fe bias; i.e., primarily because of the smaller sizes of the annuli with respect to the ASCA analysis (see section 5.1 of Buote 2000c).

4.3. The Mg/O and Si/O Discrepancies

In Figure 3 we show the O, Si, and Mg profiles obtained without deprojection (model A) and with deprojection (model C); recall that S is tied to Si in their solar ratio. The Mg and Si profiles at large radii are similar for both models. But for bins 1-3 the deprojected abundances are larger than the 2D values since the latter are lowered by the projection of lower-abundance gas from shells at larger radii. Effects related to the Fe Bias for these elements also contribute to 2D and 3D differences (Buote 2000a). (The Ne abundance is discussed below in $\S 4.5$.) Note that even though there is some blending of Fe L lines with the strongly- and He- Mg lines, the similarity of the Mg profiles to those of Si (and S), which are well separated from the Fe L lines, testifies to the reliability of the Mg abundance measurements.

The oxygen abundance exhibits very peculiar behavior. At large radius the 2D profile fluctuates considerably, while these fluctuations are reduced in the smoothed 3D profile. It is unclear as to the origin of these fluctuations, but it is likely they are the result of the background issues discussed below in $\S 4.5$. Considering this uncertainty we believe that the O abundance should be considered similar to Mg and Si at large radius.

At small radii the O abundance profile is flat having low values $Z_{\text{O}} \approx 0.2 - 0.3 Z_{\odot}$ that do not differ appreciably whether or not the spectra are deprojected. These values are quite similar to those obtained for M 87 from recent XMM analyses (Bohringer et al. 2001; Molendi & Gastaldello 2001). This flat oxygen profile is a stark contrast to the Fe, Mg, and Si profiles that all increase significantly toward the center. At these small radii possible background inaccuracies do not seriously affect the oxygen

abundances. Instead, this anomalous behavior indicates a deficiency in the standard model.

Even more "anomalous" is the Mg/O ratio at small radii. For model C we obtain Mg/O ratios (and 2 σ lower limits) of 4:5 (2:8) in bin 1 and 6:7 (4:1) in bin 2 both expressed in solar units. These values are exceptionally large when compared to Mg/O values of 0.8-0.9 solar produced by Type Ia (SN Ia) and Type II (SN II) supernovae (e.g., Gibson et al. 1997). Therefore, this presents a "Mg/O Discrepancy" between the X-ray observations using the standard model and the expectation that the metals in the hot gas are produced from previous supernova explosions.

The Si/O ratios are similarly anomalous if one also considers the Fe abundance. That is, the Si/Fe ratio of $\approx 1Z_{\odot}$ is much too large for SN Ia and therefore implies that the Si is mostly produced from SN II enrichment. If the observed Si arises from SN II then so does O because of the greater oxygen yields of SN II. But the Si/O ratio for SN II is $\approx 2Z_{\odot}$ which is less than the values of 4-6 solar in annuli 1-3 indicated in Figure 3.

4.4. Outer Annuli & Background Issues

In Figure 4 we show the spectral fits of model C for the outer annulus. It is clear that the standard model provides a good fit over much of the energy range, but the model diverges from the data toward the edges of the bandpass. We have plotted the residuals in terms of χ^2 . Expressed instead in terms of the ratio of model-to-data the residuals below 0.35 keV are $\approx 30\%$ while above 3 keV are 50%-100%.

In the outer annulus (# 9) these residuals over 0.3-0.4 keV and 3-5 keV are entirely consistent with over-subtraction of the background. The background spectrum of the MOS (and pn) CCDs is much flatter than 1 keV thermal plasma for energies above 3 keV⁷. At lower energies (< 0.7 keV) the background rises and exhibits strong K emission lines from O VII (0.56 keV) and to a lesser extent O VIII (0.65 keV). This rising background continuum at lower energies explains the residuals below 0.4 keV in annulus 9. The over-subtraction of the oxygen K lines can explain the erratic oxygen profile at large radius

⁷ See XMM calibration note by D. Lumb (XMM-SOC-CAL-TN-0016).

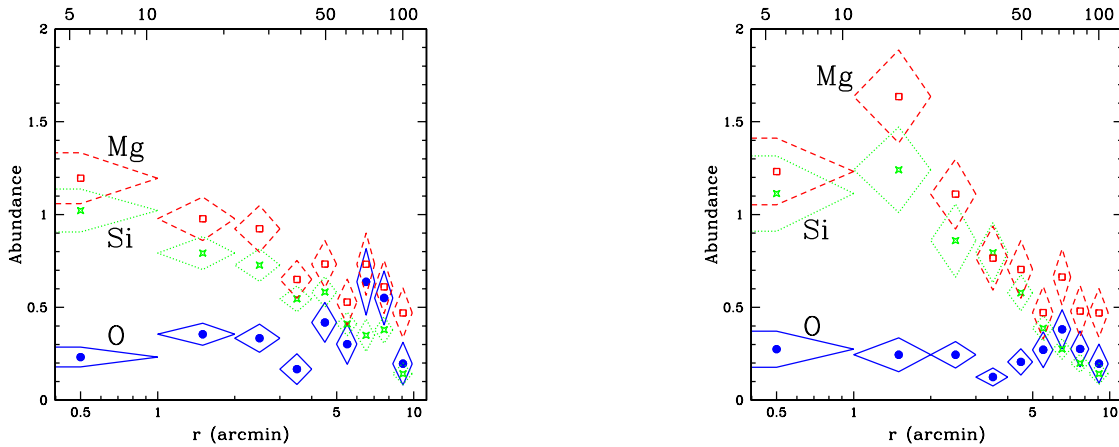


Fig. 3. (Left panel) Selected elements as a function of radius for model A and (Right panel) for model C defined in Table 1. Note that S is tied to Si in their solar ratio.

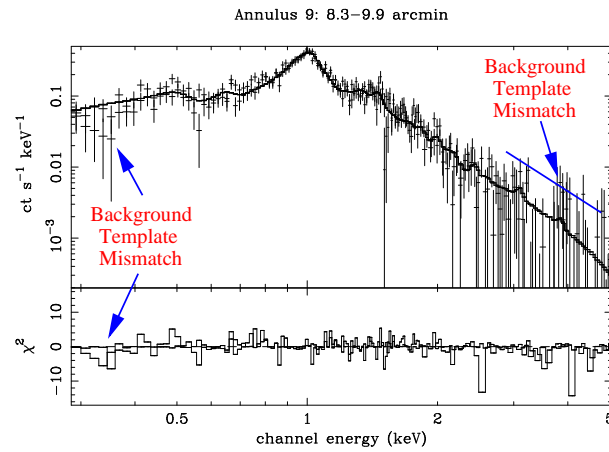


Fig. 4. Best-fitting standard model (model C, Tables 1 and 2) obtained from joint fits to the MOS1 and MOS2 (background-subtracted) data of the bounding annulus (i.e., # 9). Residuals are expressed in terms of χ^2 . Note that the spectrum is binned so that each bin contains 30 total source and background counts which is all that is required for χ^2 fitting. Since the background dominates at higher energies there are only a small number of source counts per bin there.

exhibited by the standard model in Figure 3.

Unfortunately, we cannot simply renormalize the background templates for the following reason. The large residuals over 3-5 keV do not continue to the highest energies (12 keV) of the MOS bandpass; i.e., above 5 keV there is no indication of any systematic effects of background over-subtraction. We do not expect any systematics at these higher energies because the background templates are normalized ($\times 2$) to the data between 7-12 keV (near the edge of the MOS1 and MOS2 fields). If we renormalize to better fit 3-5 keV in annulus 9 we will significantly under-subtract the background at higher energies.

It is apparent that the background templates are not a perfect representation of the spectral shape of the broadband background for NGC 5044. A perfect match is not surprising since both the cosmic and Galactic background vary with sight line and the local particle background is highly variable. The pertinent issue is how much can we trust these templates? As is clear from examination of the χ^2/dof in Table 2 the fits improve so that by annuli 6-7 formally acceptable fits are obtained with little evidence of the residuals apparent in annulus 9. And we find that temperatures and abundances (except oxygen) inferred in these annuli are not very sensitive to 10% variations in

the background normalization which represent the 3 statistical errors on the normalization. With regard to the standard model we conclude that it provides an acceptable description of the MOS data in the outer radial bins after consideration of the small mismatch of the background templates to the NGC 5044 observation.

(Note we find a more severe mismatch between background templates and the EPIC pn data which is why we do not present detailed results on the pn data at this time. However, all results obtained with the MOS in this paper are supported by the pn. We are currently investigating how to obtain a better estimate of the pn background.)

4.5. Problems in the Central Bins

Both the anomalous Mg/O ratios and large values of χ^2/dof (Table 2) within the central radial bins signify fundamental problems with the standard model. Since these problems are most severe for annulus 2 we focus our present discussion there. In Figure 5 we plot the MOS1 and MOS2 spectral data of annulus 2 and best-fitting model C. Residuals are plotted in terms of χ^2 and as a ratio of the model to the data.

The standard model provides a good qualitative fit of the MOS1 and MOS2 spectra in annulus 2. We have

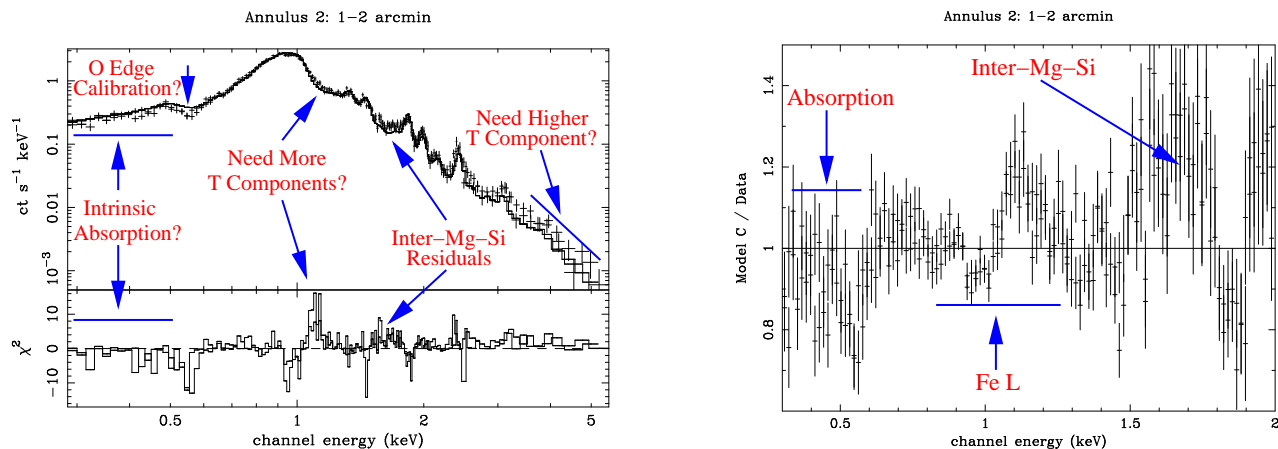


Fig. 5. (Left panel) Best-fitting model C to annulus 2 similar to that described for annulus 9 in Figure 4. (Right panel) Ratio plot of data to model where only data below 2 keV are shown.

marked on the plot the regions of the key model residuals for which we shall devote our attention. These residuals represent (see ratio plot) 10%–30% deviations. It is our intention to determine which (if any) of these key residuals are related to the physics of the source as opposed to mere errors in the calibration or plasma model codes. Calibration errors often are revealed as features that are narrower than the energy resolution, and such features are not expected to be very dependent on the position on the detector. Individual lines in the plasma codes, especially some of the strong Fe L lines, may be in error by 20%–30% in some cases as seen in high resolution RGS studies (e.g., Behar et al. 2001). However, the effect of any one line is smeared out by the moderate energy resolution of the CCDs. For example, the systematic 20%–30% positive residuals spanning 1.5–1.8 keV (i.e., 300 eV wide; Figure 5) cannot be attributed to 20%–30% errors in a few lines in the plasma codes.

First we notice that for energies > 3 keV the data lie above the model in the opposite sense to that found at large radii (x4.4). This is another indication that background issues are quite unimportant at small radii. More importantly, these high-energy deviations indicate either the fitted temperature is too low or the presence of an additional temperature component with slightly higher temperature.

Next let us consider the low-energy deviations. There appears to be a relatively sharp line absorption feature near 0.55 keV and a weaker broad underestimate below 0.5 keV. The weaker broad absorption feature below 0.5 keV is quite unlike the low-energy feature seen in annulus 9 (x4.4) that is most pronounced below 0.4 keV. Instead for annulus 2 the most significant (broad) deviations are between 0.4–0.5 keV which correspond to 10%–20% deviations. The fact that these deviations in annulus 2 are at higher energy and do not increase in magnitude with lower energy (even if energies down to 0.2 are included) strongly suggests that the background normalization is not the cause of these features.

The sharp feature near 0.55 keV is located very near the absorption edge of O I at 0.53 keV. This cannot be the result of over-subtraction of the background, since if the background is restored to the spectrum in Figure 5 the fea-

ture is hardly affected. Arguments against this being an instrumental feature are that it is observed in both MOS cameras, in the pn data, and that it is not seen at large radius. However, it might not be observed at large radius because of lower S/N. The calibration issue is difficult to assess so early in the mission, but as we discuss below (see x6.1.6 and x9.4) we favor the calibration interpretation.

We turn our attention to the "Inter-Mg-Si" residuals marked in both panels of Figure 5. By fractional deviation these are the most deviant points of the fit. These residuals connect the Mg XII Ly α line near 1.47 keV with the Si X IV He α lines near 1.85 keV. Over this energy region there are both Al and Si calibration lines in the background. But since the data lie above the model (similar to the 3–5 keV region) over-subtraction of the background cannot be the explanation. (This is further support that the background is unimportant at such small radii.) These Inter-Mg-Si residuals are particularly interesting because they could be related to the anomalous Mg/O ratios; i.e., a model that removes these residuals might naturally provide near-solar Mg/O ratios (see below in x6).

Finally, let us consider the residuals near 1 keV which are the largest in terms of χ^2 and represent 10%–20% fractional deviations. In this region the strong Fe L lines dominate the spectrum with contributions from Ni L and the Ne X Ly α line at 1.0 keV. The strong Ne X line is located right between the positive and negative residuals near 1 keV. Because of its key position we have allowed the Ne abundance to vary freely for all of the fits even though the Ne X line is strongly blended with Fe and Ni lines. Consequently, the value we derive for the Ne abundance is difficult to interpret, and thus we do not bother to regularize / smooth it like the other parameters. Allowing Ne to vary independently does not actually make much of a difference in the fits, accounting for only about 15 in χ^2 from model C in annulus 2. (From model C $Z_{Ne} = Z_{Fe} = 0.5 \pm 1$ in bins 1–2 and fluctuates between 0 and 0.5 in the other annuli.)

By letting the Ne abundance vary freely the residuals observed near 1 keV almost certainly arise from the $n = 3! 2$ Fe L lines. The fractional deviations are only 10%–20% which might not seem large considering the accuracy of the plasma code. However, the Fe L lines are

extremely sensitive to variations in temperature near 1 keV and could signal the presence of additional temperature components, a subject we address in the next section. These Fe L features are also positioned on the other side of the Mg lines opposite the Inter-Mg-Si residuals and could be partially responsible for the Mg/O problem.

Hence, both the Mg/O discrepancy and these groups of 10%–30% fractional residuals show that the standard model requires modification.

5. multitemperature models

5.1. Single-Phase Temperature Gradient

Within annulus 2 the residuals near 1 keV (Fe L lines) and 3–5 keV suggest the existence of other temperature components. However, this does not mean the assumption of a single-phase gas is in error. Notice that the deprojected models (B and C) only improve the fits over the 2D model (A) within the central three bins (Table 2). This is the region where the temperature is changing rapidly with radius, and we would expect each bin (1^o or 10 kpc wide) to contain a range of temperatures appropriate for the single-phase radial temperature gradient. For example, the best-fitting temperatures for model C are 0.74, 0.79, and 0.96 keV respectively for shells 1, 2, and 3. If we assume equal temperature spacing between bins, then for shell 2 we would estimate a temperature width of $0.875 - 0.765 = 0.11$ keV arising from the single-phase gas.

To account for the continuous range of temperatures implied by the single-phase temperature gradient while minimizing the extra number of free parameters over the standard model, we have examined spectral models having either a flat or gaussian differential emission measure (DEM). Each of these models adds just one free parameter over the standard model (a measure of the width of the DEM). Since we find that the flat and gaussian models give very similar widths and that the gaussian provides generally a better fit, we shall focus on the gaussian model.

The gaussian differential emission measure is expressed as,

$$(T) = \frac{\text{norm}}{T^2} \exp\left(-\frac{(T - T_0)^2}{2\sigma_T^2}\right); \quad (1)$$

where T_0 is the mean and σ_T the standard deviation of the gaussian, and norm is a constant proportional to $n_e n_p V$ as defined for the apec code in xspec. The luminosity over some energy range \int_E is therefore,

$$L_E = \int_E (T) (T) dT; \quad (2)$$

where $\int_E (T)$ is the plasma emissivity given by the apec code. We define model D (see Table 1) to be identical to model C for annuli 4–9 but for annuli 1–3 vapec is replaced with our local gaussian model vapec_gauss. Hence, the only parameter added over the standard model is σ_T .

The χ^2 values for model D are listed in Table 2 and the best-fitting model to annulus 2 is displayed in Figure 6. There is substantial improvement in each of the annuli 1–3, but 1–2 are improved significantly more than annulus 3. As expected, most improvement is observed for annulus 2 for which χ^2 is lowered by over 150. Also expected, as seen in Figure 6, the key improvements in the fits are in the Fe L region near 1 keV and the 3–5 keV region. Although the 3–5 keV region is now fit very well, the 1 keV

region still has notable residuals. Essentially the gaussian removed entirely the large positive residuals near 1.1 keV in Figure 5 but created some new (smaller) residuals near 0.9 keV and 1.2–1.3 keV. Nevertheless, by removing the residuals near 1 keV and 3–5 keV the use of the gaussian model verifies the hypothesis that those residuals can be explained by a finite temperature distribution within the inner annuli.

In Figure 7 we display the temperatures and selected abundances of model D compared to model C. For the temperatures of model D we have plotted only the mean, T_0 , which is similar to but slightly larger than the temperatures indicated by model C. The values of σ_T are 0.13, 0.03, 0.15, 0.03, 0.23, 0.08 keV respectively for shells 1, 2, 3. We see that bins 1–3 are spaced so that T_0 differs from its neighbors by approximately σ_T which is fully consistent with the single-phase radial temperature gradient interpretation.

The Fe abundances of model D displayed in Figure 7 exceed those of model C by 20% in shells 1–2 and by 40% in shell 3. This is simply a manifestation of the Fe bias discussed above in 4.2 and provides further illustration of the care needed in determining the Fe abundances when the temperature is near 1 keV.

The abundances of model D generally do not differ as much as the Fe abundances from model C as seen in Figure 7 for Mg and O (and Si, not shown). The largest difference is 35% observed for Mg in shell 3. Consequently, model D does not resolve the Mg/O and Si/O problems.

5.2. Multiphase Cooling Flow

Since model D does not eliminate all the residuals or solve the Mg/O and Si/O problems it is natural to examine whether the range of temperatures indicated by the gaussian instead implies a conventional multiphase cooling flow where gas cools at constant pressure. The viability of such a cooling flow model can be assessed without even performing a fit. The width of a differential emission measure can be characterized by the multiphase strength, β , which for a gaussian is $\beta = (\sigma_T/T_0)^{-2}$ (Buote et al. 1999). For model D $\beta = 0.22$ for annulus 2 which can be compared to $\beta = 0.6$ for a cooling flow with maximum temperature 1 keV (see Figure 8 of Buote et al. 1999); i.e., the differential emission measure of a cooling flow is too wide to describe the XMM data.

Direct fitting of a (3D) cooling flow model confirms that it is a very poor fit to shells 1–3. When a two-component model consisting of a cooling flow and an isothermal ambient component is fitted to the (deprojected) data in each of these shells it is always found that only the isothermal component is required in agreement with our previous ROSAT analysis (Buote 2000d). However, unlike in our previous analysis even if an intrinsic absorber is included in the fit (such as discussed below) it is still found that only the isothermal component is required by the fit.

This lack of evidence for a standard cooling flow is similar to what has been found in initial XMM observations of galaxies and clusters (e.g. Xu et al. 2001; Molendi & Pizzolato 2001; Bohringer et al. 2002).

6. intrinsic absorption models

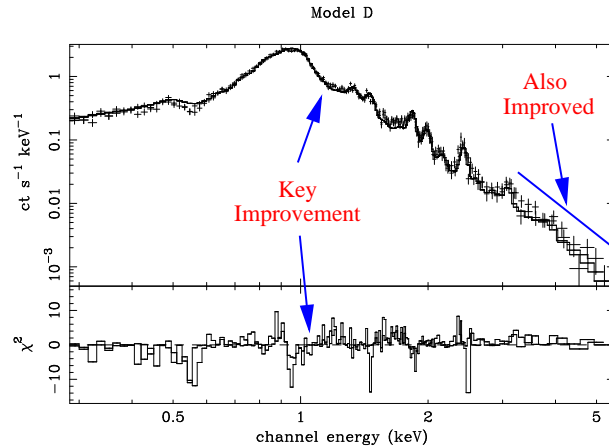


Fig. 6. | Best-fitting model D (Tables 1 and 2) to the EPIC MOS1 and MOS2 spectra of annulus 2.

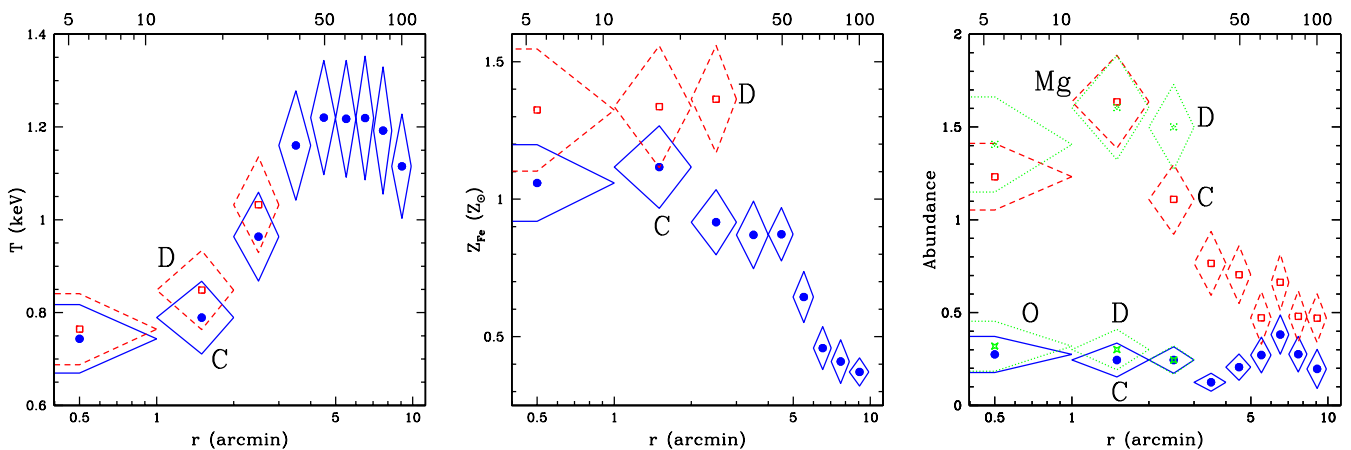


Fig. 7. | (Left panel) Radial temperature profiles (units { bottom : arcminutes, top : kpc) and 1- σ errors for models C and D defined in Table 1. (Middle panel) The iron abundance profiles of these models. (Right panel) Mg and O abundance profiles for these models.

Even after accounting for the temperature distribution arising from a single-phase temperature gradient within the central bins, the modified standard model with a Gaussian differential emission measure deviates significantly from the data both at low energies (< 0.5 keV) and in the "Inter-Mg-Si" energy region. Moreover, the Mg/O and Si/O problems remain in these central bins. We are therefore lead to consider further refinements to the standard model. Since the low-energy residuals suggest absorption in excess of the foreground contribution of the Milky Way, here we consider models of intrinsic absorption.

6.1. 2D Absorbers

In this section we consider two-dimensional absorber models where the absorber is distributed as a uniform screen placed in front of the source. By "two-dimensional" we mean that the absorption model, $A(E) = \exp(-N_H(E))$, multiplies the emission model of the entire 2D annulus in question; i.e., $A(E)$ multiplies both the emission from the 3D shell and the emission from exterior shells projected into the annulus in question. Such "2D absorption" is the typical absorber type investigated in X-ray studies of cooling flows. We discuss novel 3D absorber models below in §6.2.

6.1.1. Zero-Redshift Cold Absorber

We begin with a simple exercise to parameterize intrinsic absorption by simply allowing the column density of the zero-redshift cold absorber (i.e., phabs) to vary freely in models C and D. The χ^2 values obtained by allowing N_H to be a free parameter are listed as models E and F in Table 2; the values of N_H are listed in Figure 8. Outside $r \lesssim 5$ the column density is essentially constant with a value $N_H \approx 7 \times 10^{20} \text{ cm}^{-2}$ which is 40% larger than the Galactic value, $N_H^{\text{Gal}} \approx 5 \times 10^{20} \text{ cm}^{-2}$. At smaller radii N_H rises inward until reaching approximately a constant value in annuli 1-2 with value around $N_H \approx 11 \times 10^{20} \text{ cm}^{-2}$ (i.e., factor of 2.2 above Galactic). The excess values at large radius, certainly annuli 8-9 (and probably 7), arise from the background over-subtraction discussed earlier (§4.4). It is also worth mentioning that the excess N_H values in annuli 6-9 are also mostly eliminated if all abundances (particularly oxygen) are tied to Fe in their solar ratios.

Within the central annuli (1-3) we find that N_H is not sensitive to background normalization errors or whether or not certain abundances are varied separately from Fe; e.g., even if the background is not subtracted in annulus 2 we obtain the same fitted value of N_H . Consequently, we shall focus our discussion on these inner annuli where the need for absorption appears to be robust.

As indicated in Table 3 model E is a vast improvement over model C in annuli 1-2 and also provides significant

Table 3
Quality of Spectral Fits (χ^2/dof) for Absorption Models

Annulus	R_{in} (arcmin)	R_{out} (arcmin)	E	F	G	H	I	J
1	0.0	1.0	456.72/271	432.86/270	454.42/271	431.73/270	457.00/271	419.13/270
2	1.0	2.0	487.57/295	430.80/294	483.31/295	428.70/294	499.39/295	416.00/294
3	2.0	3.0	435.24/289	386.40/288	433.39/289	385.17/288	457.93/289	383.76/288
4	3.0	4.0	429.46/278		429.61/278		442.99/278	
5	4.0	5.0	302.18/271		295.53/271		317.25/271	
6	5.0	6.0	256.27/249		246.97/249		251.99/249	
7	6.0	7.0	274.57/246		263.23/246		265.06/246	
8	7.0	8.3	313.67/258		320.07/259		320.06/259	
9	8.3	9.9	353.01/284		359.80/285		359.80/285	

Note. | See Table 1 for the model definitions E–J.

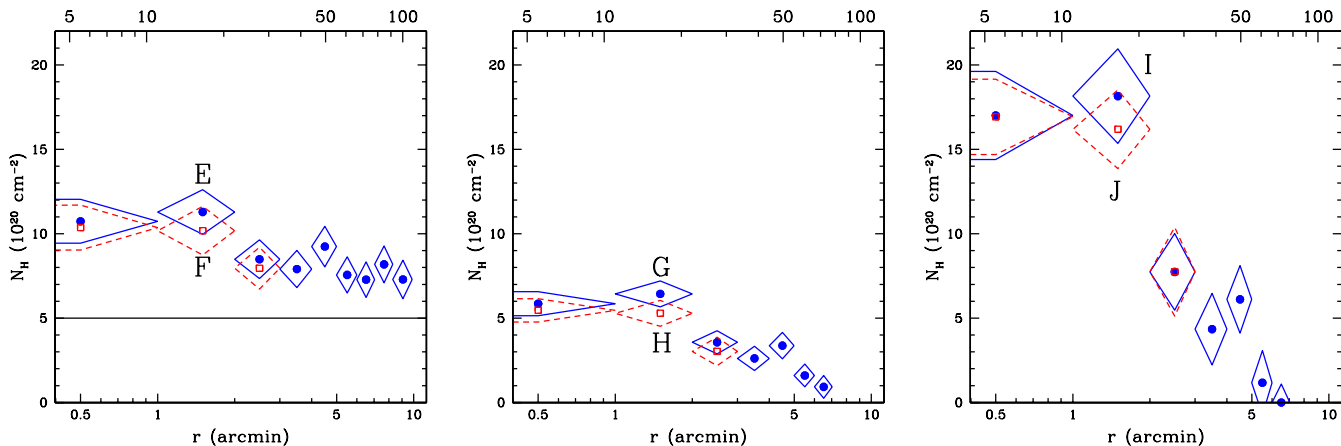


Fig. 8. | Absorption column density profiles for models in Table 3. (Left panel) Foreground cold absorber models where N_{H} is allowed to vary. Galactic value indicated by the solid horizontal line. (Middle panel) Cold absorber models in the rest frame of NGC 5044 above foreground Galactic absorption. (Right panel) Warm absorber in rest frame of NGC 5044 above foreground Galactic absorption.

improvement in bin 3. Although varying N_{H} for models with a Gaussian emission component improves the fits significantly (model F vs model D), we note that especially for annuli 1–2 the relative improvement of absorber models with and without the Gaussian (models E vs F) is considerably less than the improvement found for isothermal models with and without absorption (models E vs C). In Figure 8 it is also seen that the values of N_{H} for model F are consistent with, though perhaps slightly less than, those for model E.

The N_{H} profile of model E agrees well with that determined from the ROSAT PSPC (Buote 2000b,d) when energies below 0.5 keV were excluded from the fits to the PSPC data. The excess column densities are also similar to those obtained from multi-temperature models of the ASCA data (Buote 1999). However, unlike ROSAT, the XMM MOS data do not indicate any excess soft emission (0.2–0.3 keV) above our models in the central bins. Such soft excess emission led to sub-Galactic values of N_{H} when the PSPC data were fitted down to 0.2 keV (David et al. 1994; Buote 2000b,d). We have verified that background errors cannot resolve this discrepancy since even if we do not subtract the background in the central bins we find no evidence for significant excess soft emission. (Note that this soft excess is also not seen with the pn, but the pn does find the same excess absorption as the MOS.)

6.1.2. Intrinsic Cold and Warm Absorbers

Using phabs in models E and F we have demonstrated that absorption in excess of Galactic improves the spectral fits substantially in the central bins. Let us now consider a more realistic model of an intrinsic absorber located at the same redshift as NGC 5044 using the zphabs model in xspec. In such a model zphabs is applied in addition to the fixed Galactic absorption represented by the zero-redshift phabs model. This “cold absorber” is indicated by models G and H listed in Table 1. (By “cold” we mean that the absorbing gas consists of neutrally charged atoms implying temperatures below 10^4 K.)

We also consider “warm” absorber models motivated by our previous ROSAT studies of NGC 5044 (Buote 2000b,d). In the ROSAT studies we found that an absorber model consisting of a single absorption edge near 0.5 keV in the rest frame of NGC 5044 (i.e., oxygen edge) provided much better fits than a cold absorber. If we add such an edge to models C and D we obtain optical depth profiles that agree very well with the ROSAT data. However, a single edge is a crude phenomenological model of a warm absorber that was sufficient for the low resolution ROSAT data but not for the higher quality XMM spectra.

For our present study we constructed a detailed model of a warm absorbing gas using the ionization balance equations of Sutherland & Dopita (1993) and the photoionization cross sections of Verner et al. (1996) for elements H, He, C, N, O, Ne, Mg, Si, S, and Fe. This model has been implemented as a local xspec model (vwarmabs)

with N_H , temperature, and abundances as free parameters. The redshift is set to that of NGC 5044.

Unfortunately, allowing the different abundances to vary in the warm absorbing component (tied to their corresponding values in the emission component) is too expensive computationally for computing both best-fitting models and Monte Carlo error runs. (In the future we will seek to improve the computational efficiency of warm abs.) We therefore fixed the abundances to their solar values in the warm absorber component which we now refer to simply as warm abs (while still allowing the different abundances to vary in the emission component); for consistency of comparison we have done the same for the cold absorber component, zphabs, as well. Below in §6.1.5 we discuss differences when the absorber abundances are allowed to vary.

The temperature of the warm absorber is set to 0.01 keV determined from fits with annuli 1-2. This temperature is not well constrained such that values between 0.005-0.03 keV all give qualitatively similar fits. Note that the emission of gas at these low temperatures cannot be detected with XMM.

The χ^2 values of the cold and warm absorber models are listed as models G-J in Table 3, and the N_H values are shown in Figure 8. Because of the background issues discussed above we only apply the intrinsic absorber components to annuli 1-7. As expected, the χ^2 values of the intrinsic cold absorber (models G, H) are essentially identical to those of the zero-redshift counterparts (models E, F). Also, as expected, the values of N_H of the intrinsic absorbers derived from models G, H are essentially equal to the values obtained from models E, F minus the Galactic column.

The χ^2 values of the warm absorber without the gaussian (model I) are similar to, but slightly larger than, the corresponding cold absorber (model G). However, when the gaussian is included the warm absorber fits slightly better in the inner 2 shells (model J vs H). The column densities of the warm absorbers are larger than the cold absorbers. The maximum is always in shell 2 with value $N_H = 16 - 18 \times 10^{20} \text{ cm}^{-2}$. For both cold and warm absorbers the N_H values inferred from the gaussian emission models (H, J) are quite similar to those obtained from the isothermal models (G, I).

Let us now examine more closely why the relative quality of the fits of the cold and warm absorber changes depending on whether the gaussian emission measure is used in the central bins. In Figure 9 we plot the spectrum and best-fitting cold and warm absorber models in annulus 2 without gaussians. In comparison to the model without absorption (i.e., model C in Figure 5) the absorber models provide better fits over the whole 0.3-5 keV band. Notice first the improvement over 3-5 keV indicating that the absorber component, which itself affects directly the energies below 1 keV, allows the thermal emission component to readjust itself to fit better the higher energies. Although the temperatures in models C and G are consistent, the absorber causes the normalization (i.e., emission measure) to increase by a factor of ~ 2.3 over that obtained in model C. The increased normalization is compensated for by the intrinsic absorption at lower energies while the higher normalization at higher energies better fits the data there. In

particular, notice the superior fits of the Fe L and "Inter-M g-Si" residuals for the absorber models in comparison to model C.

As expected the absorber models improve the fits below 0.5 keV, but neither type of absorber seems to affect the narrow feature near 0.55 keV. Below 0.4 keV the residuals of the cold absorber clearly diverge near the 0.3 energy limit shown, and this continues (not shown) down to 0.2 keV. In contrast, the warm absorber produces a nearly flat residual profile down to 0.3 keV, and even fits the data well down to 0.2 keV.

Very similar results are obtained when using gaussian emission models in the central bins (Figure 10). The key difference between these models (H, J) and the isothermal models (G, I) are the slight difference in the Fe L residuals near 1 keV. Recall that model D (Figure 6), which does not include intrinsic absorption, essentially eliminates 3-5 keV residuals and the Fe L feature near 1 keV while slightly increasing Fe residuals near 0.9 keV. So when intrinsic absorption is added to model D (i.e., models H, J) the absorber component does not need to respond to χ^2 deviations at these energies and instead adjusts to fit the other parts of the spectrum, in particular the Inter-M g-Si and low-energy residuals.

Hence, based on the quality of the fits the warm absorber model is slightly preferred over the cold absorber. This conclusion assumes a preference for the gaussian emission models (H, J) since they account for the temperature distribution within shells 1-3 arising from a single-phase temperature gradient. Moreover, the low-energy data are fitted better by the warm absorber models.

It is also clear, however, the absorber components are not required only by the data at energies below 0.6 keV. Another concrete demonstration of this fact is that if we exclude the data below 0.6 keV in the fits we get very similar improvements in the fits and N_H values obtained when fitting the 0.3-5 keV spectrum. We highlight this point to emphasize that any concerns regarding background or calibration issues at low energies are quite unimportant to our basic finding that absorption models improve the fits to the XMM data in the central bins.

6.1.3. Fe Abundances

In Figure 11 we plot the Fe abundance profiles for the absorber models. Over bins 3-9 the profiles are similar for both absorber types. However, in bins 1-2 the cold absorber has $Z_{Fe} = Z_{Fe} \times 0.6 - 0.7$ compared to $Z_{Fe} = Z_{Fe} \times 1.0 - 1.2$ for the warm absorber. The warm absorber Fe abundance profile is similar to the models without intrinsic absorption. The cold absorber models appear to be either flat within $r = 5^0$ or perhaps even decreasing toward the center which would not be consistent with stellar enrichment of the hot gas. The Fe abundances of the gaussian models jump discontinuously when they arrive on the scene in annulus 3. This jump is not seen if the gaussian model is used at larger radii as well; i.e., the jump occurs simply because the gaussian always gives larger Fe abundances for these temperatures due to the Fe bias discussed earlier, and thus nothing special should be attributed to annulus 3.

6.1.4. Abundances

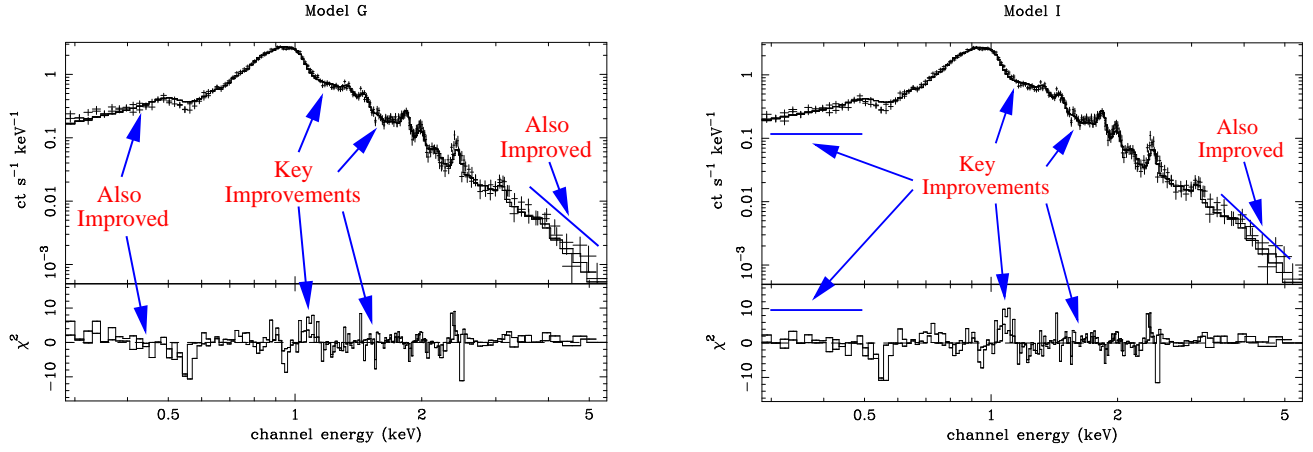


Fig. 9. | Best-fitting absorption models to annulus 2 without a Gaussian emission component: (Left panel) model G: cold absorber (Right panel) model I: warm absorber. See Tables 1 and 3.

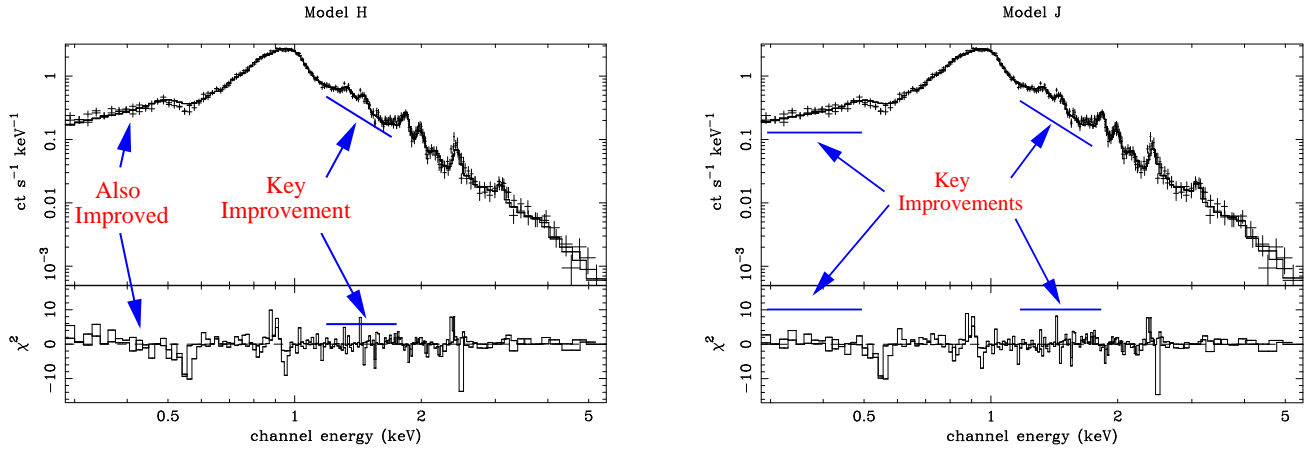


Fig. 10. | Best-fitting absorption models to annulus 2 including a Gaussian emission component: (Left panel) model H: cold absorber (Right panel) model J: warm absorber. See Tables 1 and 3.

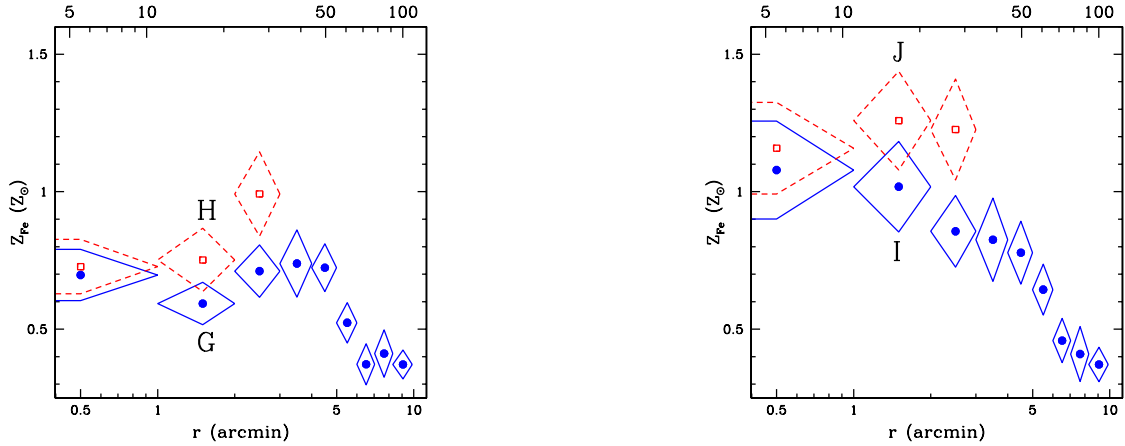


Fig. 11. | Fe abundance profiles for (Left panel) cold and (Right panel) warm absorber models in Table 3.

We plot in Figure 12 the O and Mg abundances for the absorber models. In each case the Mg abundance in the central bins is reduced significantly from those obtained from models (C,D) without absorption (cf. Figure 3). This is a consequence of the better fits to the Inter-Mg-Si spectral region by the absorber models. However, the cold absorber does not give large oxygen abundances and, in fact, gives slightly lower values than models

C and D. The result is that the cold absorber (models G and H) gives Mg/O ratios for shells 1 and 2 that are still much larger than values of around 1 solar expected from SN enrichment (see Table 4).

The warm absorber (models I and J), however, gives Mg/O values for shells 1 and 2 that are consistent with solar (see Table 4). The Mg/O ratios of 1.5–2 solar in bins 5–9 for both cold and warm absorber models are not espe-

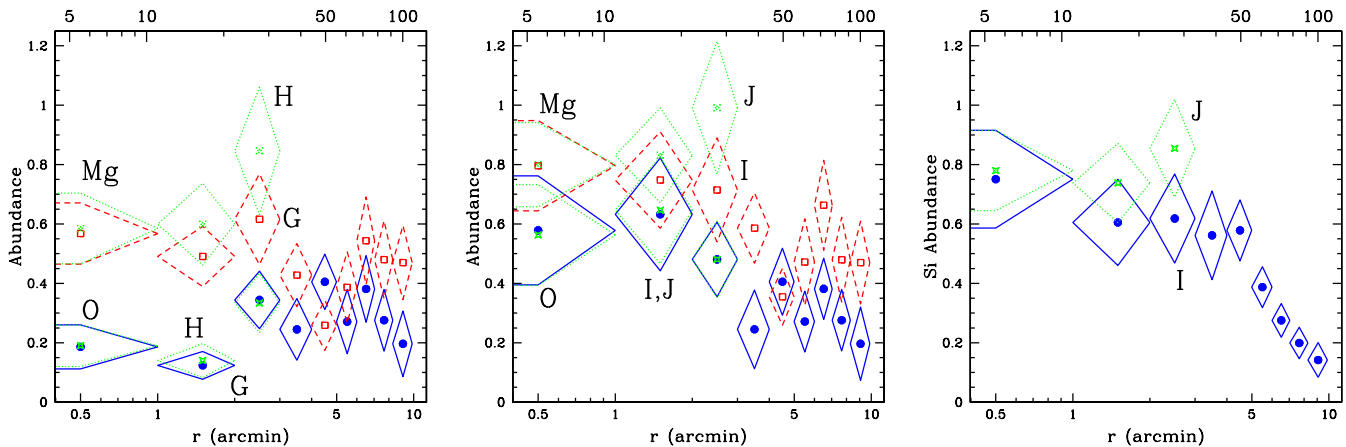


Fig. 12. | Mg and O abundance profiles for (Left panel) cold and (Middle panel) warm absorber models in Table 3. (Right panel) Si abundance profiles of warm absorbers.

Table 4
Mg/O Ratios for Selected Models

Model	Shell 1	Shell 2
C	4.5 (2.8)	6.7 (4.1)
D	4.4 (2.5)	5.3 (3.2)
G	3.0 (1.8)	4.0 (2.3)
H	3.1 (1.8)	4.3 (2.3)
I	1.4 (0.8)	1.2 (0.7)
J	1.4 (0.9)	1.3 (0.8)

Note. | Best-fitting Mg/O ratios are listed along with their 2- σ lower limits in parentheses. See Table 1 for the model definitions.

cially significant since χ^2 differences of < 10 are observed for models G–J compared to their corresponding models with O, Mg, and Si tied together in their solar ratios. The slightly larger Mg/O ratios in shell 3 (particularly for the gaussian models) are directly the result of our smoothing / regularization criterion. That is, in shell 4 oxygen ties to a low value so it cannot achieve a very high value in shell 3. If we relax the smoothing condition in shell 3 oxygen increases so that the Mg/O ratio decreases to a value consistent with those in shells 1–2.

Since only the warm absorber model gives Mg/O ratios of around 1 solar it is the only model we have explored that resolves the Mg/O problem in the central bins ($\times 4.3$). Similarly, only the warm absorbers give Si/O ratios consistent with standard SN yields. In Figure 12 we plot the Si abundance profile for the warm absorber models. As can be seen, the Si abundance is very similar to Mg (as is also true for the cold absorber { not shown) and thus gives similar near-solar ratios to oxygen.

6.1.5. Variable Abundances in the Absorber

As we noted above in $\S 6.1.2$, we do not present detailed results for absorbers with abundances tied to the emission component because of the computational expense involved in computing the errors on such models. Since, however, the computational expense for a single best-fitting model is not excessive, we have obtained best-fit results which we discuss briefly here. In particular, we have examined counterparts to models G–J where each of the abundances in the absorption component are tied to, and varied along with, the corresponding abundances of the emission com-

ponent. For a cold absorber we find that a model without a gaussian emission component in the central bins does not fit as well as model G, giving χ^2 values in the mid-500s for annuli 1–2. However, if the gaussian component is included the models fit almost identically to (slightly better than) model H. The fitted abundances of these variable-abundance cold absorbers are fully consistent with models G and H. The only notable parameter difference is that the column densities obtained are $\sim 10\%$ larger than found in models G, H.

The variable-abundance warm absorbers fit essentially the same (slightly better) for both models with and without the gaussian (models I, J). Like the cold absorber, the most notable difference between the fixed-abundance absorbers are larger column densities. In this case the N_{H} values are about 50% larger than those obtained using models I, J. (We have not yet understood in detail why the jump in N_{H} is larger relative to the cold absorbers. Undoubtedly, it is for the same reason why N_{H} for models I, J is larger than those for models G, H.) Unfortunately, we find that N_{H} and the oxygen abundance are not as well constrained for these models. However, motivated by the similar values of the abundances (Figure 12) for the fixed-abundance case, we also investigated warm absorbers where the elements are tied together as one free parameter; i.e., O, Ne, Mg, Si, and S are tied together in their solar ratios and all other elements are tied to Fe in their solar ratios (so two abundances, N_{H} and Fe, are free parameters that vary together in both the absorption and emission component). Such models give χ^2 values very similar to models I and J as expected, and yield N_{H}/Fe ratios of about

0.6 solar in the central bins.

6.1.6. Oxygen Feature

Finally, neither the cold nor warm absorber models seem to affect the narrow absorption feature near 0.55 keV. This suggests that the feature may be a calibration error, though it is curious that we do not detect it at large radius unless it is obscured there by the lower S/N data. It is also possible that modifications of our absorber models could account for this feature; e.g., an oxygen rich multiphase warm absorber. We defer consideration of such higher-order models until the calibration issue is resolved.

6.2. 3D Absorbers

We have focused our attention on 2D absorbers because the radial profile of N_H is especially sensitive to deprojection and exhibits (see below) the largest bin-bin fluctuations of any parameter. However, the quality of the fits and the values of the emission parameters (temperatures, abundances, etc.) are virtually the same for 2D and 3D absorption models. In this section we briefly discuss the 3D N_H profiles to illustrate the notable differences with respect to the 2D case.

We have modified our deprojection code to compute the effects of an intrinsic 3D absorber under various assumptions. Recall that in our 2D absorber models G–J the absorber is distributed uniformly in annuli placed in front of the source (at the source redshift); i.e., $A(E) = \exp(-N_H)$ is applied to the model of the entire spectrum in a given annulus on the sky. As a simple 3D generalization of this 2D absorber we apply $A(E)$ instead only to the emission component within the 3D shell in question, and the deprojection code takes care to add the absorption contributions from exterior shells (if any) and the foreground Galactic absorption when comparing to the entire spectrum of each annulus on the sky. In effect this 3D absorber in a given shell can be imagined (approximately) as being distributed as a uniform coating on the outer layer of that shell. (Note this procedure is employed as a convenient approximation of intrinsic absorption and is not intended to replace a full treatment of the radiative transfer which is beyond the scope of this paper.)

In Figure 13 we display the deprojected column density profiles corresponding to generalizations of models G–J; e.g., models G3D and H3D are as described for models G and H listed in Table 1 except with zphabs(2D) replaced by zphabs(3D). One immediately notices the very irregular profiles for both cold and warm absorber models exhibiting peaks in N_H for annuli 2 and 5. It is expected that these bins appear as peaks for the 3D absorber since the 2D N_H profile has similar values for bins adjacent to these peaks at smaller radii. Also expected are the smaller values of N_H in the 3D models since they refer to absorber density within the 3D radius, whereas in 2D each N_H refers to the absorption arising also from all exterior shells projected into the annulus on the sky.

We do not believe the peak in N_H in bin 5 is real. First, if we require the N_H value in bin 5 to be the same as in bin 6 we obtain a χ^2 value in bin 5 that is only about 5 larger than indicated for models E–J in Table 3 for which $\chi^2 = 300$. The resulting N_H profile increases smoothly from the outer bins through bin 5 down to bin 2. Second, we do not see the peak in bin 5 when using the pn data.

The peak in bin 2 is more significant and also appears when using the pn data. It is indeed strange why the absorber density should peak in the second bin since no such feature is apparent in the smoothly varying radial density profile of the hot gas. Also strange is that in bin 2 the electron densities (n_e) of the absorbers are quite large, being comparable to n_e in the hot gas for the cold absorber and 5 times n_e in the hot gas for the warm absorber. How such large masses of absorbing gas can be supported is unclear (cf. x9.3).

Perhaps these strange absorber features are related to peculiarities within the central lobe noted in x2. The X-ray holes evident in the Chandra image often correlate with radio jets, although there is no published radio data of sufficient quality on NGC 5044 to verify the existence of such jets. Nevertheless, these holes and the lack of evidence of cooling gas in NGC 5044 may imply feedback effects from an AGN such as proposed by Binney and others (e.g., Binney 1996). And such feedback could be responsible for the lack of absorbing gas in the central bin compared to bin 2.

On the other hand, the strange properties of the cold and especially warm absorber may imply that the models do not have any real physical meaning. Instead, they might be serving merely as parameterizations of another physical or instrumental effect that is masquerading as an absorber. Caution in the interpretation at this stage of the mission is required especially since the deviations from the standard model are only at the 10%–30% level.

7. possible non-thermal emission in central bin

We have focused on models of the thermal emission from hot gas and absorption from cold or warm material since these processes dominate the spectra over the annuli investigated. However, within the central annulus there is evidence for another emission component the origin of which is unclear.

In Figure 14 we display the MOS spectra for the central annulus (# 1) and the best-fitting warm absorber (model J). Also shown in the figure is a plot of the ratio of model J to the spectral data. There is a marked excess of the data above the model at energies above 3 keV. This high-energy excess appears in all models A–J, and it is present all the way to the upper end of the bandpass at 10 keV (not shown). This excess cannot be attributed to background error since it is not seen in the adjacent annuli. (Note that there is an excess in annulus 2 for model C shown in Figure 5 which is eliminated with a gaussian emission component to account for the temperature spread within the annulus; i.e., model D in Figure 6.)

This hard excess is modeled very well by either a simple power law or a thermal bremsstrahlung component. A power-law added to model J in Figure 14 improves the χ^2 from $\chi^2 = 419$ to $\chi^2 = 361$. The fitted parameters and 1 σ errors are $\Gamma = 2.1 \pm 0.9$ for the photon index and $(0.8 \pm 2) \times 10^4 \text{ ph cm}^{-2} \text{ s}^{-1} \text{ keV}^{-1}$ for the normalization at 1 keV. A bremsstrahlung component gives a similar improvement in the χ^2 ($\chi^2 = 357$) and yields parameters, $T = 2.6 \pm 1.3 \text{ keV}$ and normalization $(1.3 \pm 1.6) \times 10^4$ (in xspec units of emission measure). Notice that although these models clearly improve the fits their parameters are not well constrained. (We also note that the

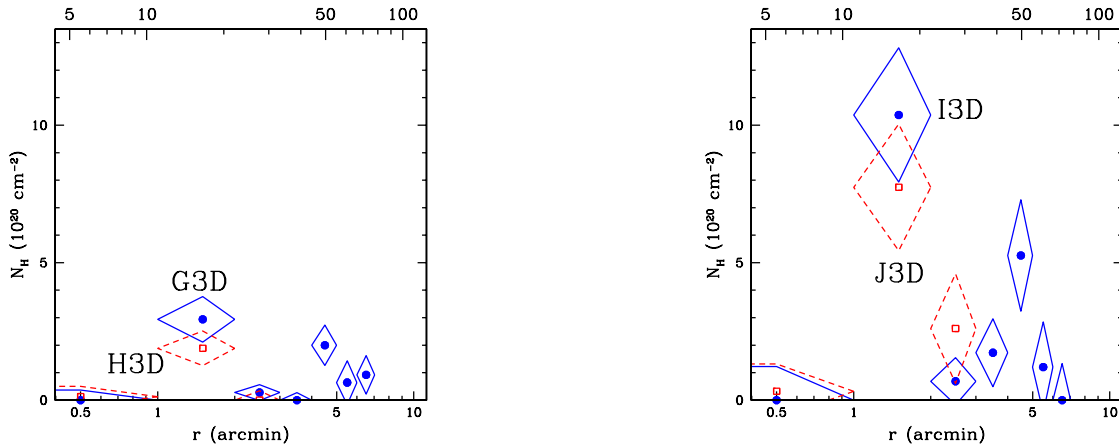


Fig. 13. Deprojected (intrinsic) absorption column density profiles for (Left panel) cold and (Right panel) warm absorber models. These models are fully analogous to models G–J listed in Table 1 except the “3D” indicates that both the absorption and emission components are simultaneously deprojected as explained in §6.2. Compare to Figure 8.

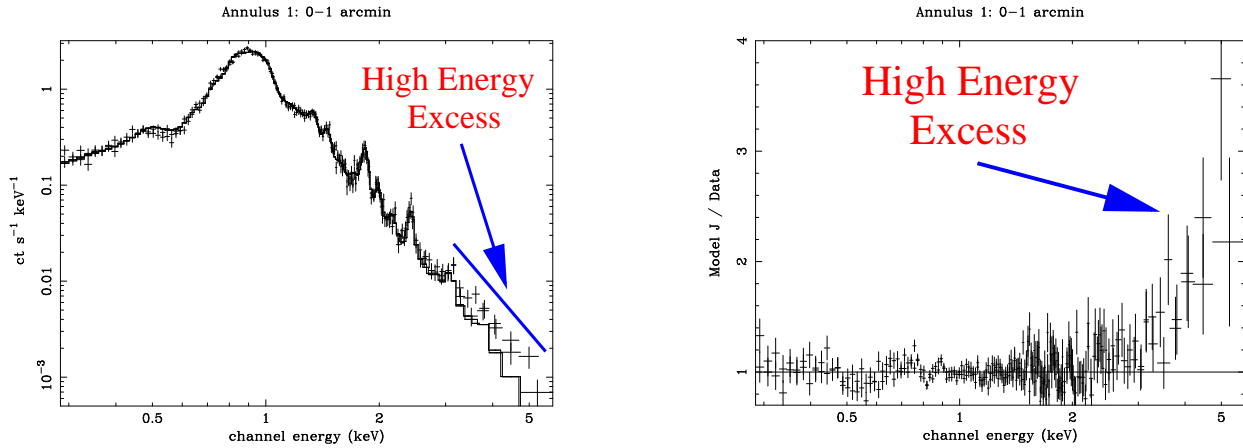


Fig. 14. Best-fitting warm absorber (model J) in the central annulus (i.e., # 1); cf. the fit for annulus 2 presented in Figure 10. This high energy excess is observed for all models A–J in annulus 1 but is not seen in the other annuli.

addition of these components does not have a strong affect on the derived parameters of the other components. However, the derived abundances in the hot gas component are systematically larger by ~20% when a power-law or bremsstrahlung component is added.)

This high energy excess is unlikely to be emission from unresolved X-ray binaries since they contribute very little flux for a source at the distance of NGC 5044. Also, the bremsstrahlung temperature of ~2 keV is less than the ~10 keV value associated with the integrated emission from X-ray binaries (e.g., Matsumoto et al. 1997).

It is tempting to associate the power-law index of ~2 with an AGN. However, inspection of the 0.3–5 keV Chandra ACIS-S image in Figure 1 does not reveal a strong central point source. If we examine the image in the 2–10 keV band to reduce the contribution from hot gas we obtain only ~10 counts for a central source within a $2''$ radius. However, the power-law and bremsstrahlung models deduced above for the XMM high-energy excess correspond to a flux of 1.8×10^{-13} erg cm $^{-2}$ s $^{-1}$ which would predict ~180 counts in the 2–10 keV band for the 20 ks ACIS-S observation. Hence, the weak point-like source at the center of NGC 5044 seen in the Chandra image cannot be responsible for the MOS hard excess displayed in

Figure 14. Instead, it may be simply the high energy tail of the emission from the hot gas.

Hence, the origin of this high energy excess in the central bin is unclear. The low resolution ($45''$) NVSS (Condon et al. 1998) radio image of NGC 5044 reveals a fairly bright central point-like source suggestive of an AGN. However, given the existence of the X-ray holes in the Chandra image it is likely that a deeper, higher resolution image will reveal extended radio emission to fill the holes. A detailed comparison of the spatial and spectral properties of the high-resolution Chandra image with a high resolution radio map may shed light on the origin of this high energy excess.

8. implications for hot gas enrichment

Two paradoxical aspects of our fits to the NGC 5044 spectrum are particularly difficult to reconcile with physical models: (1) the large mass implied by internal absorption and (2) the incompatibility of solar central metallicity with the apparent absence of cooling below 1 keV.

If warm gas with hydrogen column $N_H \sim 10^{21}$ cm $^{-2}$ is responsible for internal absorption inside $r_a \sim 20$ kpc, the mean electron density of the warm gas $n_e \sim 0.02$ cm $^{-3}$ exceeds the mean hot gas density in the same region as

noted above. It follows that the total mass of warm gas $M_w(r < r_a) \approx 10^0 M_\odot$ also exceeds that in the hot gas within r_a . How warm gas could be supported against infall in the galactic gravitational field is unclear. How the gas remains warm ($T \approx 10^3 - 10^4 K$) without rapidly cooling to much lower temperatures (in $\approx 5 - 10$ yrs) cannot be easily understood. Similar problems arise with models requiring internal absorption by cold gas. However, without internal absorption the deviations in Figure 5 remain unexplained.

Similar inconsistencies arise in reconciling the radial abundance variations observed in NGC 5044 with the absence of spectroscopic evidence of multiphase cooling below ≈ 1 keV. In the discussion below we develop a simple "no-cooling" model that illustrates this incongruity.

8.1. A No-cooling Flow

XMM observations of many other group-dominant E galaxies indicate that the gas does not cool significantly below $T \approx 10^4 K$ as predicted by traditional cooling models (e.g. Xu et al. 2001; Molendi & Pizzolato 2001; Bohringer et al. 2002). Cooling cannot be avoided if there is an extended region with net inflow (e.g. Brighenti & Mathews 2002). If gas in the central region of the flow is heated sufficiently to avoid cooling there, the inflow beyond the heated core ultimately results in compressions and radiative cooling, i.e. central heating actually induces cooling. Static solutions are unrealistic and unsatisfactory since some outflow must occur to compensate for the continuous mass ejection from the evolving old stellar population.

We consider here an idealized "no-cooling" flow which is nearly in a steady state within the central galaxy, $r < 50$ kpc. Suppose the specific stellar mass loss rate, $\dot{\rho} \approx 4.7 \times 10^{-20} s^{-1}$, is reasonably constant over several Gyrs. In addition, we assume that the hot gas density profile $\rho(r)$ does not change rapidly with time in the central galaxy. This assumption is supported by the consistent and similar stellar and X-ray surface brightness profiles in many bright E galaxies (e.g. Trinchieri et al. 1986). Cooling can be avoided only if some widespread and carefully tuned source of heating exists that compensates for the bolometric X-ray emission and drives a steady outflow, advecting the new gas to larger radii. In this case the equation of continuity $r^2 d(r^2 u) = \dot{\rho} r^2 dr$ can be solved for the outflow velocity that maintains approximately steady flow within ≈ 50 kpc:

$$u(r) = \frac{1}{r^2} \int_0^r \dot{\rho} r^2 dr = \frac{\dot{\rho} M_\odot(r)}{4 r^2} :$$

The gas density $\rho(r)$ can be found from the electron density profile, $n_e = 0.02 [1 + (r/8 \text{ kpc})^2]^{-0.6225} \text{ cm}^{-3}$, observed in NGC 5044 within ≈ 100 kpc and $M_\odot(r)$ is the de Vaucouleurs profile for NGC 5044 based on $M_{\odot,t} = 6.885 \times 10^{11} M_\odot$ and $r_e = 11.68$ kpc. This small outflow velocity, $u(r) \approx 5.0 (r_{\text{kpc}}^{0.868} + 0.4) \text{ km s}^{-1}$, maintains the observed hot gas density profile by design. If the outflow is larger (smaller) than this, the gas density (and L_x) must decrease (increase) secularly.

If the observed abundance profiles are initially imposed on this steady no-cooling flow, the abundance distributions will eventually evolve toward a steady state value as

additional metals flow from stars and supernovae. This evolution is rapid at small galactic radii (< 10 kpc) and very slow at large radii where the advection velocity is much smaller. As we show below the hot gas abundances for $r < 10$ kpc rapidly exceed those observed during this transient abundance evolution.

8.2. Iron and Silicon

For most of the spectral fits to NGC 5044 that we have considered, the Fe and Si abundances increase toward the center of the stellar image, for $r < 50$ kpc. This central peaking is most naturally understood as enrichment by Type Ia supernovae and stellar winds. A similar central SN Ia enrichment is also apparent in many other galaxy groups and clusters (e.g. Fukazawa et al. 2000). Evidently, the explosive power of Type Ia supernovae has inoculated the local hot gas with Fe, Si, S and Mg (Gibson et al. 1997).

If new metals are continuously introduced by SN Ia in the quasi-steady "no-cooling" flow described above, the abundances of Fe and Si within ≈ 10 kpc evolve toward a constant value, $Z_z(r;t) \rightarrow Z_{z,eq}$, where z represents either Fe or Si. If we assume, for example, that the initial hot gas abundance profiles $Z_z(r;0) = Z_z(r)$ are those observed in NGC 5044, after a few Gyrs the abundances will greatly exceed $Z_z(r;0)$ for $r < 10$ kpc.

To illustrate this we solve the time-dependent equation for $Z_z(r;t)$:

$$\frac{\partial Z_z}{\partial t} + \frac{1}{r^2} \frac{\partial (r^2 Z_z u)}{\partial r} = Z_{z,eq} \dot{\rho} \quad (3)$$

where

$$Z_{z,eq} = \frac{Z_{z,z}}{1.4} + \frac{y_{Fe/Ia}}{M_{sn}} \quad (4)$$

The flow velocity $u(r)$ is from the no-cooling solution and $\rho(r)$ is the observed gas density profile, both assumed to be constant for several Gyrs. Following Arimoto et al. (1997), the stellar abundance profiles in NGC 5044 are assumed to be $Z_{z,z} = Z_{z,z;0} (1 + (r/r_e)^2)^{-0.2}$ with: $Z_{z,Fe;0} = 0.75$ solar; $Z_{z,Si;0} = Z_{z,O;0} = Z_{z,Mg;0} = 1.5$ solar. The factor $1/1.4$ is needed to convert the mass of element z relative to hydrogen to the mass of z per unit total mass. The mass of Type Ia supernovae is $M_{sn} = 1.4 M_\odot$ and the specific supernova rate \dot{M}_{sn} corresponds to 0.06 SN Ia per $10^{10} L_B$ per 100 years, about 40 percent of the value suggested by Cappellaro & Turatto (2002) for $H_0 = 70 \text{ km s}^{-1} \text{ Mpc}^{-1}$. We assume yields of $y_{Fe/Ia} = 0.744$, $y_{Si/Ia} = 0.16$, $y_{O/Ia} = 0.15$ and $y_{Mg/Ia} = 0.009$, all in M_\odot .

The light curves in Figure 14 show parameterized approximations to the Fe and Si abundance variations $Z_z(r;0)$ observed in NGC 5044 (model J). The heavy curves show the abundance profiles of these elements 3 Gyrs later as evolved by the equation above. Even after only 3 Gyrs the hot gas abundance of Fe and Si within about 5 kpc are 3.35- and 2.5 times solar, far in excess of those observed in NGC 5044 or in any other similar galaxy. In order to match the observed abundances in this region, the SN Ia rate would need to be ≈ 0.01 SNu, less than 10% of the value suggested by Cappellaro & Turatto (2002) and the stellar abundances would need to be lower by at least a factor of 2. Outward advection by $u(r)$ plays only a minor role in the solution, so it is clear that our particular

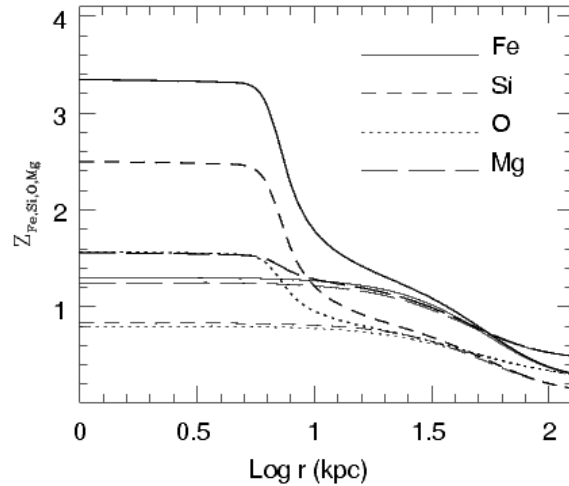


Fig. 15. | Abundance profiles in the no-cooling flow model for NGC 5044. Light lines: Approximate initial profiles for Fe, Si, O and Mg based on Model J; Heavy lines: Abundance profiles in the no-cooling flow 3 Gyr later.

assumption of steady flow has little influence on the rapid growth of iron and silicon in the central region.

In traditional cooling in flow models with dropout, iron and silicon are continuously removed in the cooled gas and it is relatively easy to find solutions with peaked abundance profiles that agree with those observed; this is possible using astronomically acceptable τ and \dot{m}_{sn} . But in mildly outflowing flows, such as our no-cooling solution, the abundances of Fe and Si increase toward $Z_{z,req} = Z_z(r; 0)$. This result is similar to the argument of Loewenstein & Mathews (1991) and Ciotti et al. (1991).

If the iron and silicon from SN Ia fail to mix thoroughly with the ambient hot gas, these regions could cool so fast that little line emission would result (Fujita et al. 1997; Morris & Fabian 2001). However, it seems likely that the supernova ejecta would be well mixed and diluted by Rayleigh-Taylor instabilities. Indeed, in successful models of Milky Way enrichment it is usually assumed that Type Ia enrichment products are efficiently distributed into the interstellar gas where they form into subsequent, metal-enriched stellar generations.

8.3. Oxygen and Magnesium

Both O and Mg are produced almost exclusively in Type II supernovae (e.g. Gibson et al. 1997). Consequently, we expect that any central enhancement of these elements in the hot gas is a result of stellar mass loss from the old stellar population, which was enriched by SN II events when the galaxies formed.

Mg and O abundances are expected to track each other rather closely in the ejecta of normal Type II supernovae. Both elements are formed in the envelopes of massive stars during the pre-supernova period so their post-supernova yields should reflect this well-understood phase of stellar evolution (e.g. Rauscher et al. 2001; Heger et al. 2002). However, if the energy released during SN II explosions is much larger than previously thought, as in so-called "hypernovae", further explosive nucleosynthesis can occur as the stronger blast wave propagates through the stellar envelope, processing oxygen to heavier elements and reduc-

ing its yield relative to magnesium (e.g. Nomoto et al. 2001).

In models A and C or D without internal absorption (Figure 3) the hot gas Mg abundance increases toward the center of NGC 5044. This is expected if the stellar Mg abundance also increases there and if the stellar ejecta merge with the hot gas. Supersolar stellar Mg abundances and strong galactic gradients are directly observed in the starlight of most massive E galaxies similar to NGC 5044 (Trager et al. 2000b,a), and central Mg peaks could be easily understood if the hot gas was globally inflowing with multiphase cooling. If the O abundance of the stars varied with galactic radius like Mg and other alpha elements, a strong central O peak would also be expected. Such a rise in the O abundance toward small radii does occur in the hot gas in M 87/Virgo in the preferred models of Melendi & Gastaldello (2001), although the O abundance slightly decreases within about 2.5 kpc where the central AGN makes the interpretation more difficult. In M 87/Virgo the O abundance is also lower than expected, $0.4 - 0.5$ solar. Nevertheless, M 87/Virgo provides some evidence that the enrichment by stellar mass loss is conveyed to the ambient hot gas. However, for NGC 5044 a central peak in the O abundance only occurs in model J as a consequence of internal absorption by warm gas. The central O and Mg abundances also experience unrealistic transient growth in our no-cooling solution as shown in Figure 14.

We conclude that either some unknown agency is masquerading as warm gas absorption so that the O abundance in NGC 5044 is truly peaked, or that the mean stellar O abundance in NGC 5044 is unusually low, ~ 0.25 solar. This could occur, for example, if the O created in early SN II events was mostly delivered to the surrounding hot gas and did not cool to form later generations of stars. By this hypothesis, the low O abundance does not necessarily require hypernovae, since the O ejected in SN II is simply diluted to ~ 0.25 solar by primordial gas. Because oxygen is further out in the pre-SN II stellar envelope, it will be more strongly shock-heated than the deeper Si and Fe zones, perhaps increasing the probability that the O

will continue to reside mostly in the (slowly cooling) hot gas phase.

At present we know very little about the stellar O abundance in giant E galaxies. The stellar TiO bands are more a measure of Ti than O since the abundance of Ti is so low. Because of the LINER spectrum, there is no $\lambda 4363$ [O III] emission from the diffuse H II gas in E galaxies, even in M 87 (Dopita et al. 1997). The central depletion of O in M 87, which has been interpreted as line absorption by some continuous X-ray opacity (Mathews et al. 2001), could in principle result from a low stellar O abundance there, which dilutes the central hot gas. Finally, we note that there is already some evidence that the stellar O abundance is low in (otherwise) super-metal-rich stellar populations. Studies of planetary nebulae in the M 31 bulge suggest low O (Jacoby & Ciardullo 1999), and the planetaries in the giant E galaxy Cen A have mean O abundances of 0.3 solar despite the metal-rich stellar content there (Walsh et al. 1999).

9. conclusions

We present a detailed initial study of a new XMM observation of the bright nearby galaxy group NGC 5044, which has been previously classified as a massive cooling flow by ROSAT and ASCA studies (David et al. 1994; Buote 1999). The XMM EPIC MOS and pn images are dominated by the diffuse emission from hot gas which fills the entire EPIC fields. Several point sources are visible embedded in the diffuse emission, and are most prominent at larger radii where the surface brightness of the diffuse emission is weakest. Within a 1° radius the emission displays asymmetries which the archival Chandra image reveals to be holes similar to those seen in other cooling flows.

To obtain the three-dimensional properties of the X-ray emitting gas we perform a deprojection analysis assuming spherical symmetry using the (non-parametric) "onion-peeling" technique. The assumption of spherical symmetry is justified by the nearly round X-ray image of NGC 5044 outside of the central 1° . We emphasize that ours is a true 3D analysis where the spectral model of a given 3D shell ($r_{i-1}; r_i$) is fitted directly to the XMM spectrum within the corresponding 2D annulus ($R_{i-1} = r_{i-1}; R_i = r_i$) on the sky minus the spectral contributions (emission and any intrinsic absorption) projected into the 2D annulus from exterior shells ($r_{j-1} > r_i; r_j$). Other methods that infer 3D spectral parameters simply by performing a typical 2D spectral analysis and then afterwards deprojecting the 2D parameters are still subjected to fitting biases like the Fe Bias (Buote 2000a,c).

9.1. Evidence for Single-Phase Gas

Assuming a single-phase gas in each spatial bin we find that the 3D temperature profile rises outwards from a minimum of $T = 0.75$ keV at the center to a maximum of $T = 1.2$ keV at $r = 50$ kpc and then declines slowly until reaching a value of $T = 1.1$ keV at $r = 100$ kpc. This 3D profile is quite similar to that we derived previously from the ROSAT data (Buote 2000c). For $r < 30$ kpc, where the temperature is changing rapidly, the spectral fits assuming one temperature component per spatial bin are considerably worse if the spectra are not deprojected.

This indicates that the range of temperatures within these 3D shells is smaller than within the corresponding 2D annuli as is expected from projection effects associated with a radial temperature gradient of a single-phase gas. (If, instead, each 3D shell contains a wide range of temperatures from, say, a multiphase cooling flow, then deprojection would have not obviously provided a better fit for a single-temperature model.)

We have found additional support for the single-phase interpretation from consideration of simple multi-temperature models within the central bins. In particular, using a gaussian emission measure instead of a single-temperature model improves the fits substantially within the central

30 kpc. The gaussian temperature widths obtained from the fits are $T = 0.15 - 0.2$ keV which are quite similar to the differences between the gaussian mean temperatures in these bins; i.e., the range of temperatures implied by the gaussian models is consistent with the small range of temperatures expected in each 3D shell from the radial temperature variation of the single-phase model. Moreover, the small values of τ imply "multiphase strengths" (Buote et al. 1999) much smaller than standard models of multiphase cooling flows cooling at constant pressure; direct fitting of such cooling flow models confirms they do not fit nearly as well as gaussian or single-temperature models. Therefore, the XMM data strongly favor single-phase models of the hot gas and demonstrate that the multi-temperature models required by large-aperture ASCA data reflect a radially varying single-phase temperature profile, a consistency that was established previously from joint ROSAT and ASCA analysis of NGC 5044 and other elliptical galaxies / galaxy groups (Buote 1999).

The apparent absence of multiphase cooling in NGC 5044 is incompatible with traditional gas dynamical models that are globally flowing inward (see x8).

9.2. Abundances and Implications

The Fe abundance exhibits a prominent gradient where $Z_{\text{Fe}} = 1Z$ near the center and falls to $Z_{\text{Fe}} = 0.35Z$ in the bounding shell near a radius of 100 kpc. (Fe abundances quoted with respect to the meteoritic solar value.) The near-solar values obtained with XMM within a radius of 5° (50 kpc) confirm that previous very sub-solar Fe abundances obtained for NGC 5044 are the result of the "Fe Bias" (see Buote 2000a,c). We have also reproduced the results of previous ASCA studies and demonstrated explicitly the Fe Bias for NGC 5044 by fitting models to the MOS spectra accumulated within a circle of radius 5° .

Consequently, the "Iron Discrepancy" raised by Arimoto et al. (1997) for elliptical galaxies (and applies also to central-E-dominated groups) is partially attributed to the incorrect measurements of X-ray Fe abundances due to the Fe Bias. A contributing factor to the "Iron Discrepancy" is the theoretical overestimate of expected Fe values due to the neglect of primordial gas during galaxy formation (Brighenti & Mathews 1999). In particular, we find that the modest central metal enrichment observed in NGC 5044 is incompatible with outflowing gas dynamical models (see x8).

Models without intrinsic absorption give Mg/O ratios of $5 - 7$ solar in the central bins which substantially exceed the values of 0.8-0.9 solar predicted by both SN Ia

and SN II. (The Si/O ratios are also too large for the measured Si/Fe ratio.) A cold absorber model slightly decreases the Mg/O ratios to $\sim 3-4$ solar primarily by setting lower Mg abundances but not affecting the very sub-solar oxygen abundances in the center. Only a warm absorber ($T \sim 0.01$ keV) gives Mg/O ratios near solar ($\sim 1.2-1.4$ solar) consistent with SN enrichment (as well as consistent Si/O and Si/Fe ratios). The success of the warm absorber model is manifested not only by lowering the Mg abundance but also by increasing the oxygen abundance to $Z_{\text{O}} \sim 0.6Z$ in the central bins.

9.3. Problems with Warm Absorbers

Warm ($T \sim 0.01$ keV) absorbers provide the best fits to the XMM spectra and are the only models that give Mg/O (and Si/O) ratios consistent with SN enrichment. However, it is difficult to understand physically the origin of this warm gas and how it is maintained at these temperatures where the cooling time is so short. Of course it is tempting to associate the warm gas with matter that has cooled out of the hot phase. But there is no evidence for multiphase hot emission components in the central bins and certainly no evidence for a standard cooling flow with gas cooling at constant pressure. In particular, there is no 0.57 keV O VII He- line expected from $T \sim 0.1$ keV gas intermediate between the warm and hot phases. Hence, if cooling of the hot gas is responsible for the warm absorber the gas must be cooling in a very different manner than is usually assumed.

The existence of gas cooler than the hot phase in the central regions of NGC 5044 is not so unusual since it is known to have substantial diffuse emission extending out at least to a radius of 0.5° (Machetto et al. 1996). Perhaps the $T = 10^4$ K H α gas and the $T = 10^5$ K warm-absorber gas have a common origin and are heated and supported by the same unknown mechanism. The X-ray holes seen in the Chandra ACIS-S image within the central arc minute are similar to those seen in other groups and clusters which some have attributed to AGN feedback in response to the cooling gas. AGN heating perhaps could account for the heating of the H α and warm gas, but it does not explain why there is no gas emitting at temperatures between the hot and warm phases. And the excess high energy emission seen in the central bin does not support the AGN hypothesis since it does not originate from a central point source ($\times 7$).

It is also frustrating that there is no "smoking gun" feature in the X-ray band that will definitively test the warm absorber hypothesis. The temperature ($T \sim 0.01$ keV) is too low for detection of the emission from this component in X-rays. (FUV space observatories are perhaps the only hope here, and there is a report of a detection of O VII emission

in at least one cooling flow by Bragman et al. (2001).) Furthermore, the absorption spectrum of warm gas arises from series of edges from several elements appearing essentially as continuous absorption even at high resolution; i.e., there is no dominant isolated spectral feature. The absorption is even "softer" if, as expected, the warm gas is multi-temperature so that many edges from each element make significant contributions to the absorption.

We recognize that the strange properties of the warm absorber may imply that it is not physical. Rather, the warm absorber might be serving merely as a surrogate for another physical or instrumental effect that is masquerading as an absorber. Further work on NGC 5044 and related systems is clearly required.

9.4. Possible Errors in Calibration and Plasma Codes

We have identified a narrow feature near 0.55 keV ($\times 6.1.6$) that cannot be accounted for by any of our models, including those with absorption. This feature is likely associated with residual error in the calibration of the oxygen edge in the MOS detectors. However, we note that this feature is only detected in the central bins.

The need for intrinsic absorption in our models arises primarily from the data between $0.6-1$ keV (not the data below 0.5 keV where the calibration is less secure). The calibration of the relative effective area of the CCDs is accurate to better than 5% (Lumb 2002) and thus cannot be responsible for the absorption.

Because of the problems with a warm absorber model noted above, it is essential to verify the accuracy of the Fe L lines in the plasma codes at the relatively cool temperatures ($0.7-1$ keV) of galaxy groups. The strong Fe L lines near 0.7 keV are known to be inaccurate in the *apec* code (e.g., Behar et al. 2001). However, it seems unlikely that these lines are responsible for the absorption since no large residuals are seen at 0.7 keV for any of our models. Moreover, since we find no qualitative differences between results obtained with the *apec* and *mekal* codes, it is clear that the need for an absorber is not sensitive to small differences in the assumptions in the atomic physics for the plasma codes.

This work is based on observations obtained with XMM, an ESA science mission with instruments and contributions directly funded by ESA Member States and the USA (NASA). We gratefully acknowledge partial support from NASA grant NAG 5-9956 for the analysis of the XMM observation of NGC 5044. Studies of the evolution of hot gas in elliptical galaxies at UC Santa Cruz are supported by NASA grant NAG 5-3060 and NSF grant AST-9802994 for which we are very grateful. FB is supported in part by grants MURST-CO 00 and ASIARS99-74.

REFERENCES

- Anders, E. & Grevesse, N. 1989, *Geochim. Cosmochim. Acta*, 53, 197
 Arimoto, N., Matsushita, K., Ishimaru, Y., Ohashi, T., & Renzini, A. 1997, *ApJ*, 477, 128
 Aumaud, K. A. 1996, in *ASP Conf. Ser. 101: Astronomical Data Analysis Software and Systems V*, Vol. 5, 17
 Behar, E., Cottam, J., & Kahn, S. M. 2001, *ApJ*, 548, 966
 Böhringer, H., et al., 2001, *A & A*, 365, L181
 Böhringer, H., Matsushita, K., Churazov, E., Ikebe, Y., & Chen, Y. 2002, *A & A*, submitted (astro-ph/0111112)
 Binney, J. J. 1996, in *Gravitational dynamics*, 89{101
 Bragman, J. N., Miller, E. D., & Irwin, J. A. 2001, *ApJ*, 553, L125
 Brighenti, F. & Mathews, W. G. 1999, *ApJ*, 515, 542
 | .2002, *ApJ*, submitted (astro-ph/0111112)
 Buote, D. A. 1999, *MNRAS*, 309, 685
 | .2000a, *MNRAS*, 311, 176
 | .2000b, *ApJ*, 532, L113
 | .2000c, *ApJ*, 539, 172
 | .2000d, *ApJ*, 544, 242

- Buote, D. A., Canizares, C. R., & Fabian, A. C. 1999, *MNRAS*, 310, 483
- Buote, D. A. & Fabian, A. C. 1998, *MNRAS*, 296, 977
- Cappellaro, E. & Turatto, M. 2002, (astro-ph/0012455)
- Churazov, E., Brüggen, M., Kaiser, C. R., Böhringer, H., & Forman, W. 2001, *ApJ*, 554, 261
- Ciotti, L., Pellegrini, S., Renzini, A., & Decrocco, A. 1991, *ApJ*, 376, 380
- Condon, J. J., Cotton, W. D., Greisen, E. W., Yin, Q. F., Perley, R. A., Taylor, G. B., & Broderick, J. J. 1997, *AJ*, 115, 1693
- Davids, L. P., Jones, C., Forman, W., & Daines, S. 1994, *ApJ*, 428, 544
- Dopita, M. A., Koratkar, A. P., Allen, M. G., Tsvetanov, Z. I., Ford, H. C., Bicknell, G. V., & Sutherland, R. S. 1997, *ApJ*, 490, 202
- Fabian, A. C., Sanders, J. S., Ettori, S., Taylor, G. B., Allen, S. W., Crawford, C. S., Iwasawa, K., Johnstone, R. M., & Ogle, P. M. 2000, *MNRAS*, 318, L65
- Finoguenov, A. & Ponman, T. J. 1999, *MNRAS*, 305, 325
- Fujita, Y., Fukumoto, J., & Okoshi, K. 1997, *ApJ*, 488, 585
- Fukazawa, Y., Makishima, K., Matsushita, K., Yamasaki, N., Ohashi, T., Murozumi, R. F., Sakima, Y., Tsuchida, Y., & Yamashita, K. 1996, *PA SJ*, 48, 395
- Fukazawa, Y., Makishima, K., Tamura, T., Nakazawa, K., Ezawa, H., Ikebe, Y., Kikuchi, K., & Ohashi, T. 2000, *MNRAS*, 313, 21
- Gibson, B. K., Loewenstein, M., & Murozumi, R. F. 1997, *MNRAS*, 290, 623
- Heger, A., Woosley, S. E., Rauscher, T., Hoeman, R. D., & Boyce, M. 2002, *New Astronomy Reviews*, in press (astro-ph/0110015)
- Ishimaru, Y. & Arimoto, N. 1997, *PA SJ*, 49, 1
- Jacoby, G. H. & Ciardullo, R. 1999, *ApJ*, 515, 169
- Loewenstein, M. & Mathews, W. G. 1991, *ApJ*, 373, 445
- Lumb, D. 2002, preprint (astro-ph/0203276)
- Macchetto, F., Pastoriza, M., Caon, N., Sparks, W. B., Giavalisco, M., Bender, R., & Capaccioli, M. 1996, *A&AS*, 120, 463
- Mathews, W. G., Buote, D. A., & Brighenti, F. 2001, *ApJ*, 550, L31
- Matsushita, K., Koyama, K., Awaki, H., Tsuru, T., Loewenstein, M., & Matsushita, K. 2001, *ApJ*, 482, 133
- McNamara, B. R., Wise, M., Nulsen, P. E. J., Davids, L. P., Sarazin, C. L., Bautz, M., Markevitch, M., Vikhlinin, A., Forman, W. R., Jones, C., & Harris, D. E. 2000, *ApJ*, 534, L135
- McWilliam, A. 1997, *ARA&A*, 35, 503
- Molendi, S. & Gastaldello, F. 2001, *A&A*, 375, L14
- Molendi, S. & Pizzolato, F. 2001, *ApJ*, 560, 194
- Morris, R. G. & Fabian, A. C. 2001, in press (astro-ph/0108091)
- Nomoto, K., Maeda, K., & Umeda, H. 2001, in press (astro-ph/0110528)
- Rauscher, T., Heger, A., Hoeman, R. D., & Woosley, S. E. 2001, *ApJ*, submitted (astro-ph/0112478)
- Renzini, A. 1997, *ApJ*, 488, 35
- Struder, L., et al. 2001, *A&A*, 365, L18
- Sutherland, R. S. & Dopita, M. A. 1993, *ApJS*, 88, 253
- Trager, S. C., Faber, S. M., Worthey, G., & Gonzalez, J. J. 2000a, *AJ*, 120, 165
- Trager, S. C., Faber, S. M., Worthey, G., & Gonzalez, J. J. 2000b, *AJ*, 119, 1645
- Trinchieri, G., Fabbiano, G., & Canizares, C. R. 1986, *ApJ*, 310, 637
- Vemer, D. A., Ferland, G. J., Korista, K. T., & Yakovlev, D. G. 1996, *ApJ*, 465, 487
- Walsh, J. R., Walton, N. A., Jacoby, G. H., & Peletier, R. F. 1999, *A&A*, 346, 753
- Wyse, R. F. G. 1997, *ApJ*, 490, L69
- Xu, H., Kahn, S. M., Peterson, J. R., Behar, E., Paerels, F. B. S., Murozumi, R. F., Jemigan, J. G., & Makishima, K. 2001, *ApJ*, submitted (astro-ph/0110013)